Petroleum Science 23 (2026) 2622–2638

Contents lists available at ScienceDirect

Petroleum Science

journal homepage: www.keaipublishing.com/en/journals/petroleum-science

Original Paper

# Fracture propagation mechanisms of cross-layer fracturing with directional perforation in off-target horizontal wells

Xiao-Hua Wang [a], Liu-Ke Huang [b,*], Chang-Heng Li [c], An-An Wu [c], Sheng-Rong Zhu [b], Li Qian [d], Kuan Lu [e]

[a] Department of Geotechnical Engineering, College of Civil Engineering, Tongji University, Shanghai, 200092, China
[b] School of Civil Engineering and Geomatics, Southwest Petroleum University, Chengdu, 610500, Sichuan, China
[c] Oil and Gas Technology Research Institute, PetroChina Changqing Oilfield Company, Xi'an, 710021, Shaanxi, China
[d] Technical Consulting Center, PetroChina Southwest Oil & Gasfield Company, Chengdu, 610017, Sichuan, China
[e] CNOOC Tianjin Branch, Tianjin, 300452, China

ARTICLE INFO

*Article history:*
Received 7 September 2025
Received in revised form
20 January 2026
Accepted 21 January 2026
Available online 25 January 2026

Edited by Jia-Jia Fei

*Keywords:*
Cross-layer fracturing
Directional perforation
Fracture propagation
Horizontal well
Unconventional resources

ABSTRACT

Multi-stage fracturing with horizontal wells is a pivotal technique for developing the unconventional reservoirs. Owing to complex geological conditions coupled with inherent limitations in existing drilling technologies, a significant proportion of horizontal wellbores deviate from the target reservoir, instead inadvertently penetrating adjacent upper and lower interlayers. These misplaced sections are termed the non-reservoir horizontal wellbore intervals (NRHWI). In this scenario, the cross-layer fracturing with directional perforation (CLFDP) is introduced as an effective stimulation method. Despite its potential, the mechanisms governing fracture initiation and propagation in CLFDP operations remain poorly understood. This study, therefore, develops a three-dimensional (3D) numerical model of CLFDP for Well H in the Changqing Oilfield, China. The model specifically considers a horizontal wellbore positioned within the mudstone interlayer overlying the target sandstone reservoir and incorporates realistic perforation geometry. We systematically investigate fracture morphological characteristics, injection pressure dynamics, and fracture area evolution. The goal is to examine how these parameters are influenced by variations in wellbore location, perforation depth, and perforation spacing. The results demonstrate that a distinctive gourd-shaped fracture yields in the CLFDP case. The horizontal wellbore trajectory should be optimally steered to maximize reservoir contact, leveraging advanced technologies such as rotary steering systems—a critical factor in enhancing stimulation efficiency. In scenarios where the horizontal wellbore deviates from the target reservoir, we recommend employing deep-penetration perforation (with large perforation depth) combined with high-density perforation (reduced perforation spacing) to effectively develop the NRHWI. These outcomes provide essential theoretical underpinnings and technical support to maximally harness the unconventional resources.


## 1. Introduction

Against the backdrop of escalating global energy demands and the accelerated depletion of conventional hydrocarbon reserves, the exploitation of unconventional oil and gas resources, including tight sandstone and shale, has emerged as a critical component in maintaining energy security (Blunt et al., 2025; Wang et al., 2026; Yin et al., 2025a, 2025b; Liu et al., 2023). The unconventional resources have the geological characteristics of low permeability (usually less than 0.1 mD) and low porosity (usually less than 10%) (Huang et al., 2019, 2022, 2025b; Wang et al., 2022b; Zhao et al., 2023). The multi-stage fracturing with horizontal well is the key technology to attain economically viable production for these resources (Tang et al., 2024; Wang et al., 2025; You et al., 2025; Zhang F. et al., 2025; Zhou et al., 2025). However, engineering practice demonstrates that due to complex underground conditions and inherent limitations in existing drilling techniques, a

* Corresponding author.
*E-mail address:* swpuhlk@126.com (L.-K. Huang).
Peer review under the responsibility of China University of Petroleum (Beijing).

https://doi.org/10.1016/j.petsci.2026.01.037

significant portion of horizontal wellbore trajectories frequently deviate from the target reservoir. The wellbore mistakenly penetrates non-reservoir formations such as adjacent upper and lower interlayers (Luo et al., 2016). This errant section is termed the non-reservoir horizontal well interval (NRHWI). In early development, the NRHWI is excluded from fracturing operations, rendering a substantial portion of the wellbore being abandoned, and it obviously leads to considerable resource wastage. Unlocking the productivity potential of NRHWI through technological innovation has emerged as a critical challenge in achieving efficient development of unconventional reservoirs.

Therefore, the cross-layer fracturing with directional perforation (CLFDP) is introduced in an attempt to effectively stimulate the NRHWI (Bai et al., 2021; Li et al., 2023; Pidho et al., 2022; Xi et al., 2022). This approach leverages the steering capability of perforation tunnels to guide the propagation of hydraulic fractures initiated from interlayers. This guidance enables them to promptly propagate toward the target reservoirs and ultimately facilitating efficient stimulation. Currently, scholars have systematically investigated the propagation mechanisms of hydraulic fractures induced by directional perforation through multidisciplinary approaches encompassing theoretical analysis, laboratory experiments, and numerical simulations (Dong and Li, 2025). In the realm of theoretical research, a study was conducted to explore the impact of wellbore deformation, which resulted in the introduction of a novel approach for calculating fracture pressure within perforated elliptical wellbores (Ren et al., 2022). Their findings underscored an optimal perforation depth ranging from roughly 1.5 to 2 times the wellbore's dimensions. To address the prediction of initiation parameters, a semi-empirical method was introduced for assessing both the pressure and orientation of fractures in directional perforations (Michael and Gupta, 2021). This approach is formulated based on fracture initiation data collected from seven high-yield shale gas production blocks. They emphasized that directional perforation strategy holds significant potential for optimizing fracturing treatment by promoting lateral fracture initiation or suppressing treatment pressure. Research into directional perforation design led to the development of a computational framework for determining the associated breakdown pressure and optimal orientation (Xia et al., 2025). Their model incorporates casing-cement interaction effects and perforation quality. Furthermore, they proposed a novel perforation cluster layout designed to optimize fracture initiation.

In laboratory experiments, large-scale fracturing experiments to investigate the fracture propagation in vertical wells with directional perforation were conducted (Chen et al., 2010). They revealed that the directional perforation generates complex curved fractures, with the curvature being influenced by the perforation angle and the horizontal stress differential. Using concrete casting, specimens with oriented perforations were fabricated and subsequently subjected to fracturing experiments (Shi et al., 2021). They revealed that a transverse fan-shaped fractures is created for oriented perforation, whereas the branched and tortuous fractures are formed for spiral perforation.

In numerical simulations, a fluid-solid coupling stress model specific to directional perforation was developed (Liu et al., 2015). Their work provided an initiation pressure determination method and analyzed fracture characteristics under various in-situ stress states, including the normal and reverse fault types. To predict the initiation pressure in directional perforation, a stress distribution model was derived that incorporated the effects of casing, perforation, and fluid (Zeng et al., 2019). Their results demonstrated that while in-situ stress significantly influences initiation pressure, its effect on optimal perforation orientation is relatively minor. The two-dimensional deflection of symmetrically distributed fractures in directional perforation has been systematically investigated in previous studies (He et al., 2021; Lu et al., 2022; Wang et al., 2024; Zhang et al., 2020). The extended finite element method is employed to model the fracture propagation for directional perforation, taking into account the effects of perforation azimuth and confining pressure (Liu et al., 2020). Their findings indicated that the challenges associated with fracture initiation and deflection became more pronounced as the azimuth angle increased, while they diminished with a rise in the confining pressure ratio coefficient. Additionally, recent studies applying the continuous-discontinuous element method has shown that specific perforation patterns, including spiral, linear, and symmetrical, are critical factors influencing fracture geometry and initiation pressure (Li et al., 2024; Zhang et al., 2024).

The aforementioned studies elucidate the propagation dynamics of hydraulic fractures in the context of directional perforation. Nevertheless, there remains a notable scarcity of numerical simulations that explicitly incorporate the geometry of actual perforation tunnels. In current research, perforation clusters containing multiple tunnels are commonly simplified as line segments (in 2D models) or planar fractures (in 3D models). Such simplifications inherently preclude the consideration of how perforation parameters, including perforation depth and perforation spacing, influence fracture propagation. Moreover, the effect of varying horizontal wellbore positions within interlayers relative to the target reservoir is still poorly understood, which limits the optimal selection of fracturing intervals. Consequently, this study employs the development of tight oil reservoirs in Well H, located within China's Changqing Oilfield, as the engineering context. Leveraging the discrete lattice method, we construct a three-dimensional numerical model for CLFDP that uniquely accounts for the actual distribution of perforation tunnels. This approach enables a detailed investigation into the effects of horizontal wellbore position, perforation depth, and perforation spacing on fracture behavior. The findings provide a theoretical foundation for improving the effectiveness of unconventional hydrocarbon recovery through NRHWI, thereby enhancing overall recovery efficiency.

## 2. Background and method

### 2.1. Engineering background

The Well H, situated in the Yishan slope of the Ordos Basin in China's Changqing Oilfield. The target reservoir is the tight sandstone reservoir with an average buried depth of −2023.47 m and a pore pressure of 19.91 MPa. The vertical, maximum horizontal and minimum horizontal stresses of the reservoir are 46.13, 35.58, and 30.37 MPa, respectively, resulting in a horizontal stress difference of 5.21 MPa. The mudstone layers are present in both the upper and lower parts of the sandstone reservoir. The vertical, maximum horizontal and minimum horizontal stresses of the mudstone layers measure 46.68, 42.16, and 37.26 MPa, respectively. The Well H is developed utilizing the multi-stage fracturing with horizontal well, featuring a horizontal wellbore length of 2068.43 m. During the drilling of horizontal wellbores, a significant proportion fail to pass through the target reservoir. Instead, they mistakenly penetrate adjacent upper and lower interlayers. This occurs due to complex underground conditions and the inherent limitations of existing drilling technologies. For example, the length of the horizontal wellbore in Well H encountering the sandstone reservoir constitutes approximately 64.7% of the entire horizontal wellbore length, as shown in Fig. 1. Therefore, on-site engineers propose the CLFDP, aiming to effectively stimulate the NRHWI. The Well H serves as a pioneering test well for CLFDP operations in the

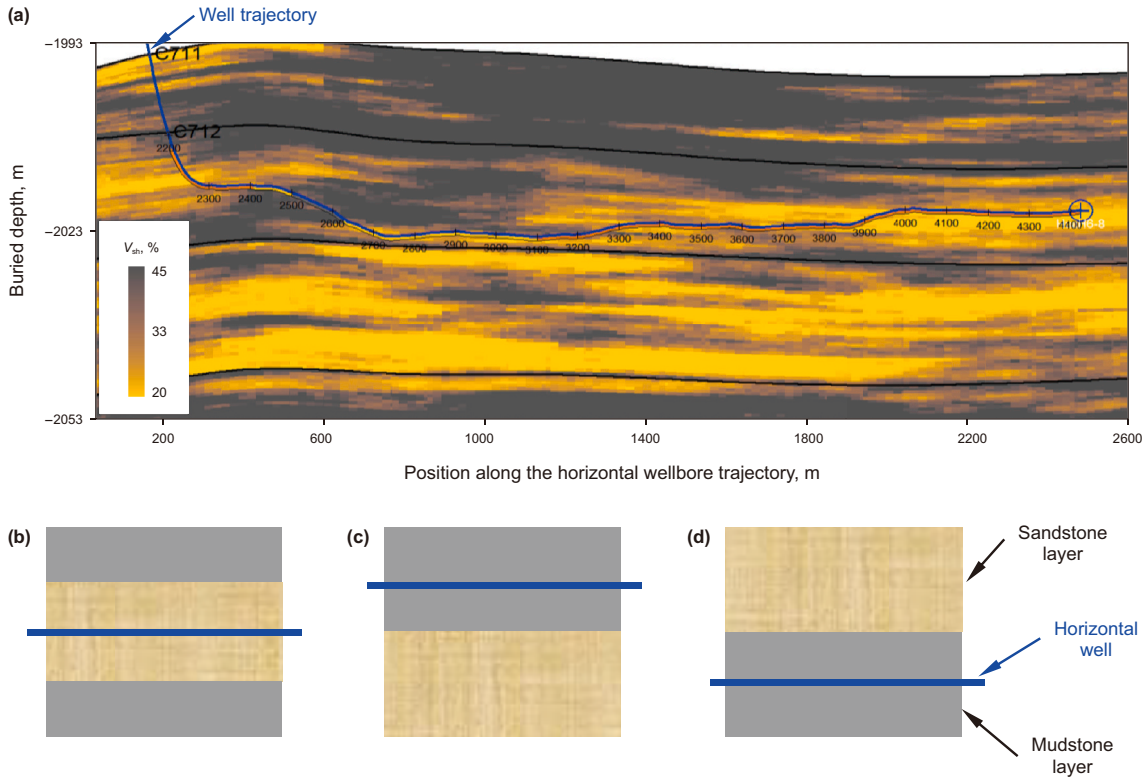


**Fig. 1.** (**a**) Distribution of sandstone and mudstone along the horizontal wellbore trajectory of Well H. The $V_{sh}$ denotes the content of mudstone. The blue line illustrates the well trajectory. Schematic diagram illustrating different crossing modes of the horizontal wellbore trajectory within the formations, including (**b**) the horizontal wellbore traversing inside the target sandstone reservoir, (**c**) the horizontal wellbore crossing within the mudstone layer above the target reservoir, and (**d**) the horizontal wellbore passing through the mudstone layer below the target reservoir.

Changqing Oilfield. Therefore, this paper investigates the fracture propagation in CLFDP through numerical simulation, aiming to provide theoretical insights for the design optimization of such structures.

### 2.2. Research method

In the lattice method, the contacts between the nodes are represented by springs (Fig. 2). The fluid elements are situated at the mid-points of the springs. The interconnections between these fluid elements are termed flow pipes, and they correspond to permeable contacts (such as fractures generation) between the nodes (Huang et al., 2024, 2023; Tang et al., 2023; Wang et al., 2023b; Wu et al., 2021; Zhang et al., 2021; Zhang et al., 2024). When multiple pipes are interconnected, they collectively form a fluid pipe network. Within this network, both pore pressure diffusion and fluid flow take place. The pipe network undergoes evolution in tandem with the progression of damage in the mechanical model. As new fluid elements emerge at the sites of newly formed microfractures, they integrate with pre-existing fluid elements, thereby forging new conduits and dynamically updating the pipe network (Huang et al., 2025a; Wang et al., 2023a).

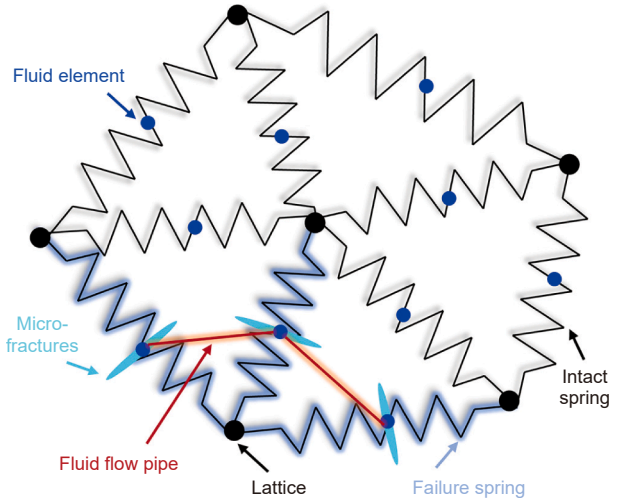


**Fig. 2.** Schematic illustration of the discrete lattice.

The discrete lattice method utilizes an explicit solution scheme, with the translational degrees of freedom at each node being discretized using the central difference formula (Damjanac et al., 2011, 2016; Damjanac and Cundall, 2016):

$$\begin{cases} \dot{u}_i^{\left(t+\frac{\Delta t}{2}\right)} = \dot{u}_i^{\left(t-\frac{\Delta t}{2}\right)} + \sum \frac{F_i^{(t)}\Delta t}{m} \\ u_i^{(t+\Delta t)} = u_i^{(t)} + \dot{u}_i^{\left(t+\frac{\Delta t}{2}\right)}\Delta t \end{cases} \tag{1}$$

where $\dot{u}_i^{(t)}$ and $\dot{u}_i^{(t+\Delta t/2)}$ represent the velocity components in the $i$ direction ($i = 1,3$) at time $t$ and $t + \Delta t/2$ respectively, $\sum F_i$ denotes the resultant force in all $i$ directions ($i = 1,3$), $m$ is the node mass, and $\Delta t$ indicates the time increment.

At time $t$, the component of angular velocity ($w_i$) in the $i$ direction ($i = 1, 3$) is (Damjanac et al., 2011, 2016; Damjanac and Cundall, 2016):

$$w_i^{\left(t+\frac{\Delta t}{2}\right)} = w_i^{\left(t-\frac{\Delta t}{2}\right)} + \frac{\sum M_i^{(t)}}{I}\Delta t \tag{2}$$

where $\sum M_i^{(t)}$ is the sum of the moments acting on all $i$ components ($i = 1,3$) of the node at time $t$, and $I$ is the moment of inertia of the node.

The spring's normal ($F^N$) and tangential ($F^S$) forces are (Damjanac et al., 2011, 2016; Damjanac and Cundall, 2016):

$$\begin{cases} F_i^N \leftarrow F_i^N + \dot{u}_i^N K^N \Delta t \\ F_i^S \leftarrow F_i^S + \dot{u}_i^S K^S \Delta t \end{cases} \tag{3}$$

where $K^N$ is the normal stiffness, and $K^S$ is the tangential stiffness.

Then the new spring forces are added into the sum of the forces at the relevant nodes (Damjanac et al., 2011, 2016; Damjanac and Cundall, 2016):

$$\begin{cases} \sum F_i^A \leftarrow \sum F_i^A - F^N n_i - F_i^S \\ \sum F_i^B \leftarrow \sum F_i^B + F^N n_i + F_i^S \end{cases} \tag{4}$$

where $n_i$ is the unit normal vector from node $A$ to node $B$.

Once the spring sustains damage, microcracks will emerge, causing the spring force to revert to zero, as indicated by $F^N = 0$ and $F^S = 0$. In addition, the tensile and shear strengths of micro springs correspond to these of macro rock masses as follows (Damjanac and Cundall, 2016):

$$\begin{cases} F^{N\,\max} = \alpha_t T R^2 \\ F^{S\,\max} = \mu_f F^{N\,\max} + \alpha_s C R^2 \end{cases} \tag{5}$$

where $F^{N\,\max}$ is the tensile strength of the spring, $F^{S\,\max}$ is the shear strength of the spring, $\alpha_t$ is the calibration coefficient for tensile strength, $\alpha_s$ is the calibration coefficient for shear strength, $T$ is the tensile strength of the macroscopic rock mass, $C$ is the shear strength of the macroscopic rock mass, $R$ is the resolution, and $\mu_f$ is the friction coefficient.

Assuming the pipe's width is equivalent to its length, the flow rate from fluid elements $A$ to $B$ along the pipeline is (Damjanac et al., 2011, 2016):

$$q = \beta k_r \frac{a^3}{12\mu}\left[p^A - p^B + \rho_w g\left(z^A - z^B\right)\right] \tag{6}$$

where $a$ is the fracture width, $\mu$ is the fluid viscosity, $p^A$ and $p^B$ represent the fluid pressure of fluid elements $A$ and $B$, $z^A$ and $z^B$ are the water head of fluid elements A and B, $\rho_w$ is the fluid density, $\beta$ is the calibration parameter.

The relative permeability $k_r$ is a function of saturation $s$ (Damjanac et al., 2011, 2016; Damjanac and Cundall, 2016):

$$k_r = s^2(3 - 2s) \tag{7}$$

Obviously, when the pipe is saturated (i.e. $s = 1$), and the relative permeability is 1. Explicit numerical methods are adopted to solve the temporal evolution of fluid flow. The fluid pressure increment $\Delta p$ (Damjanac et al., 2011, 2016; Damjanac and Cundall, 2016) is:

$$\Delta p = \frac{\sum q_i}{V}\overline{K}_F \Delta t_f \tag{8}$$

where $\overline{K}_F$ represents the apparent fluid bulk modulus, $V$ denotes the element volume, $q_i$ is the injection rate of the pipe connected to element $i$, and $\Delta t_f$ indicates the flow time step.

The rock mechanics model and fluid flow model are fully coupled to achieve an integrated fluid-solid interaction process (Damjanac et al., 2011, 2016; Damjanac and Cundall, 2016; Wang et al., 2022a). Fluid flow dynamics are primarily governed by the system's permeability characteristics. When fluids propagate through either stress-induced fractures or pre-existing fracture networks, the resulting fluid pressure exerts normal and shear stresses on fracture surfaces, consequently influencing rock deformation and mechanical strength. Conversely, rock deformation induces dynamic variations in both fluid pressure and fracture aperture, leading to permeability evolution within the fracture system. It is noted that unlike the particle flow code (PFC), the discrete lattice model requires input parameters that are macroscopic mechanical and physical properties of the rock, such as the elastic modulus, Poisson's ratio, and compressive strength, rather than the microscopic properties of the micro-scale particle or contact. These input macroscopic parameters are directly converted into corresponding micro-properties, which are then mapped and assigned to the masses and springs in the model. This method avoids the need for complex manual calibration of microscopic parameters (i.e., there is no calibration process for lattice strength mapping coefficients), thereby eliminating subjectivity in parameter calibration at the source and ensuring consistency between the macroscopic mechanical behavior and the input parameters.

## 3. Numerical modelling

### 3.1. Model establishment

Fig. 3 displays a numerical model of CLFDP for a certain horizontal wellbore section deviating from the sandstone reservoir in Well H. The numerical model is constructed based on the actual wellbore dimension, perforation size and layout of Well H in the Changqing Oilfield. However, due to the millimeter-scale perforations, decimeter-scale wellbore, and meter-scale near-wellbore region, the minimum resolution (i.e., mesh size) in the numerical model is constrained by the perforation size. This leads to a substantial number of nodes and a considerable reduction in computational efficiency, thereby limiting the model dimensions. In this situation, while striving to maintain acceptable computational efficiency, we maximize the model size as much as possible. The final model dimensions are determined to be 6.10 m (length) × 6.10 m (height) × 1.83 m (width), comprising approximately 1.56 million nodes. A single simulation typically requires about 45 h to complete on an Intel® Core(TM) i9-14900K 3.20 GHz workstation. Therefore, the current model size represents a compromise between computational resources and simulation accuracy, and serves as the principal basis for model size selection. Moreover, both the overlying mudstone and underlying sandstone layers exhibit a thickness of 3.05 m, respectively. The mechanical properties, physical characteristics, and in-situ stresses of the two layers are summarized in Table 1. It is noted that the vertical stress of the mudstone layer is even greater than that of the sandstone layer. The reason is: The study area is located in the Ordos Basin, China, and is influenced by tectonic compression. As a result, the vertical stress is not solely governed by the overlying strata, but is

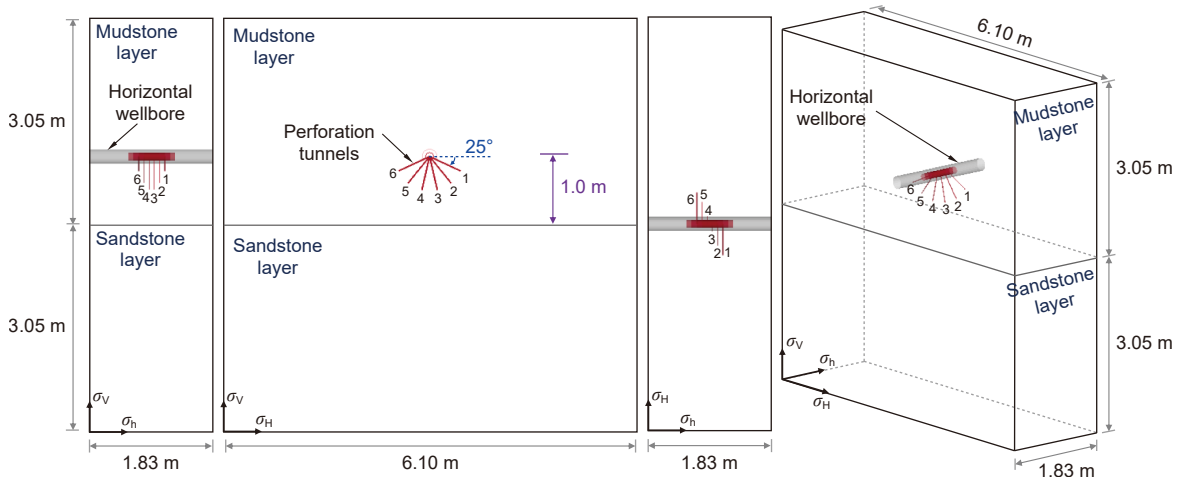


**Fig. 3.** Numerical model of cross-layer fracturing with directional perforation.

**Table 1**
Mechanical properties, physical parameters, and in-situ stresses of mudstone and sandstone layers.

| Parameters | Mudstone layer | Sandstone reservoir |
|---|---|---|
| Elastic modulus, GPa | 31.29 | 23.15 |
| Poisson's ratio | 0.32 | 0.26 |
| Uniaxial compressive strength, MPa | 109.52 | 84.97 |
| Density, kg/m$^3$ | 2634.16 | 2448.27 |
| Tensile strength, MPa | 4.45 | 2.03 |
| Vertical stress, MPa | 46.68 | 46.13 |
| Maximum horizontal principal stress, MPa | 42.16 | 35.58 |
| Minimum horizontal principal stress, MPa | 37.26 | 30.37 |
| Porosity, % | 3.09 | 6.71 |
| Permeability, mD | 0.02 | 0.08 |

also affected by horizontal tectonic forces. As shown in Table 1, the maximum and minimum horizontal stresses in the mudstone layer are higher than those in the sandstone layer, indicating that the mudstone is generally under a higher stress state. This may be attributed to structural compression or lithological densification. In such a tectonic setting, vertical stress can be increased through the Poisson effect, which helps explain the observed phenomenon of slightly higher vertical stress in the mudstone layer.

The injection rate of the fracturing fluid is maintained at 0.1 m$^3$/min with a viscosity of 2.5 mPa·s, and the fluid leak-off is neglected. The horizontal wellbore, featuring a radius of 106.35 mm, is positioned 1.0 m above the stratigraphic interface. Six perforation tunnels are arranged in a helical configuration along the wellbore, each with a radius of 7.50 mm and a length of 0.5 m. The perforation pattern begins (i.e. the first perforation tunnel) with an initial inclination of 25° relative to the horizontal plane, with subsequent tunnels spaced at 26° phase angle intervals around the wellbore. Furthermore, the constant stress boundary conditions, including the vertical stress, the maximum and the minimum horizontal stresses (Table 1), are applied. These conditions are chosen to realistically represent the constant far-field stresses in actual geological settings. A no-flow boundary condition is applied to the boundary of the model. Notably, in the current numerical model, we adopt a simplified approach by assuming uniform fluid pressure at each perforation tunnel, without accounting for frictional losses of the fracturing fluid when flowing through the wellbore and perforation channels. In fact, frictional losses during fluid flow can result in pressure variations among perforations, which in turn influence fracture initiation at individual tunnels and ultimately affect the overall fracture propagation. Therefore, in our subsequent work, we will incorporate fluid frictional losses into an extended version of the model. This may involve integrating computational fluid dynamics modules to enable a more comprehensive evaluation of fracture initiation and propagation during perforated fracturing. These improvements are expected to enhance both the practical applicability and predictive accuracy of the model.

### 3.2. Model validation

Firstly, we conduct numerical simulations of a penny-shaped fracture and compare the geometric solution obtained from the simulations with the theoretical solution proposed by Dontsov (2016). The mechanics parameters and physical properties used in the simulation are listed in Table 1. The injection rate is 0.1 m$^3$/min, the fluid viscosity is 2.5 mPa·s, and the injection duration is 1680 ms. Fig. 4(a) displays the simulated fracture morphology, which resembles the shape of a coin. In Fig. 4(b), the numerical solution is depicted by black dots, its fitting outcome is illustrated by the solid black line, and the theoretical solution is signified by the red solid line. Results indicate the numerical solution forms a discrete distribution closely approximating the theoretical solution, and the excellent agreement between the fitted results and theoretical predictions occurs. This confirms that the discrete lattice method effectively simulates fracture propagation under the geological parameters and engineering conditions specified in Section 3.1.

Moreover, we discuss the effects of three different mesh sizes (i.e., resolutions), such as the coarse resolution of 8.22 mm, the medium resolution of 5.87 mm, and the fine resolution of 4.19 mm. It is found that, compared with the theoretical solution, the relative errors of the maximum fracture length and width for the fine-

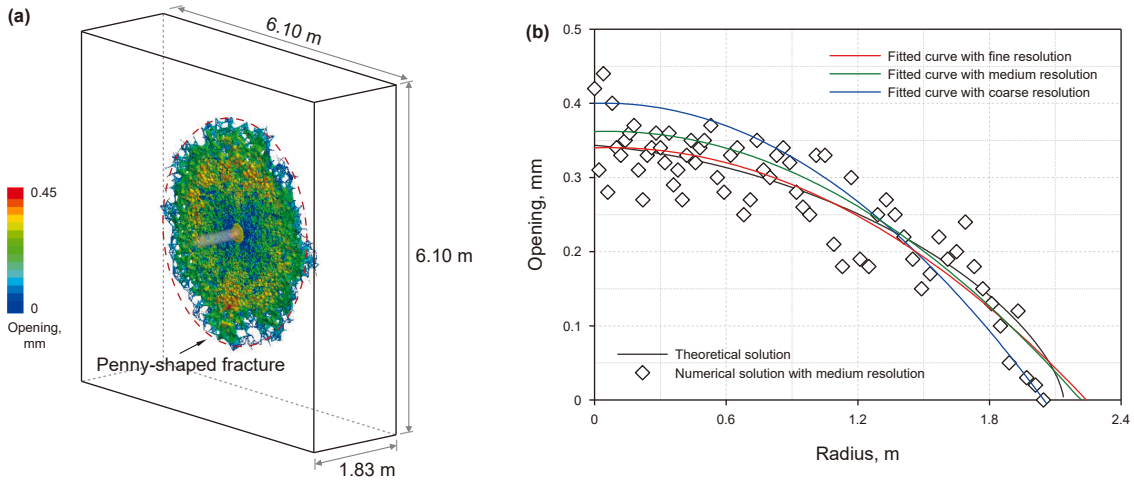


**Fig. 4.** (**a**) Penny-shaped fracture obtained from the numerical simulation, and (**b**) comparison between numerical and theoretical solutions.

resolution case are −1.01% and 4.82%, respectively; for the medium-resolution case, they are 5.4% and 2.95%, respectively; and for the coarse-resolution case, they are 16.46% and −4.54%, respectively (Fig. 4(b)). It is observed that the simulation results under fine resolution are closer to the theoretical solution. However, when the resolution is improved from 4.19 to 5.87 mm, the deviation of the numerical results remains relatively small, indicating that under the studied conditions, the fracture propagation simulation using the discrete lattice method exhibits mesh independence. Considering the trade-off between computational cost and accuracy, this study selects the medium resolution (5.87 mm) for subsequent simulations.

Fig. 5 presents a comparative analysis of the injection pressures between on-site CLFDP of Well H and the numerical results. The simulated pressure trend aligns closely with the field-observed pressure data. Notably, the measured on-site breakdown pressure is 48.44 MPa, while the numerical modeling predicts a breakdown pressure of 50.89 MPa, yielding a deviation of 5.06% (2.45 MPa). Similarly, the field-measured average extension pressure of 36.44 MPa closely matched the simulated value of 36.74 MPa, with a negligible discrepancy of 0.82%. These findings validate the reliability of the CLFDP model developed in this study.

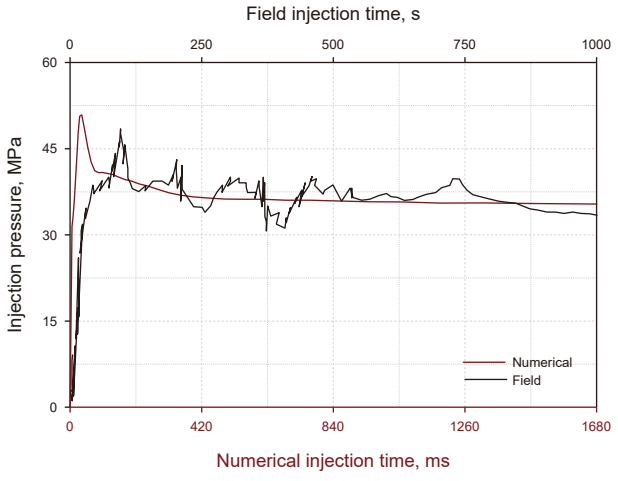


**Fig. 5.** Comparison between on-site and numerical simulation injection pressures for CLFDP of Well H.

### 3.3. Simulation results

Fig. 6 displays the fracture morphologies of CLFDP evolving with varying injection durations. Hydraulic fractures firstly initiate from each perforation tunnel (30 ms) and subsequently extend radially, resulting in the formation of planar fractures that are perpendicular to the direction of the minimum horizontal stress along the entire tunnels. These planar fractures propagate independently (60 ms). Following this, the fractures from adjacent tunnels begin to partially coalesce, gradually giving rise to a transverse main fracture perpendicular to the horizontal wellbore (120 ms). Once hydraulic fractures propagate into the lower sandstone layer (after 300 ms), they exhibit rapid and preferential extension in the sandstone layer, while their growth in the upper mudstone layer is significantly inhibited, progressing at a much slower rate. Ultimately, this results in the formation of a gourd-shaped hydraulic fracture (1680 ms), characterized by a limited propagation in the mudstone layer and an extensive propagation within the sandstone layer. In addition, hydraulic fractures in the mudstone layer exhibit gaps in the upper half of the wellbore. This phenomenon is attributed to the directional perforation wherein the perforation tunnels are predominantly clustered towards the lower part of the wellbore, instead of being evenly distributed around it. In addition, we can observe that during the initial stage of hydraulic fracture propagation (at 30 ms), the fracture opening is very small. As the hydraulic fracture continues to extend, the crack width increases significantly. Interestingly, when the fractures propagate from the mudstone layer into the sandstone layer (at 300 ms), the fracture width within the sandstone becomes markedly larger than that within the mudstone, resulting in a noticeable contrast in width between the two layers. This difference is primarily attributed to the higher elastic modulus of the mudstone compared to the sandstone.

Fig. 7 illustrates the evolution of injection pressure and fracture area, as derived from quantitative statistics of CLFDP simulation. The total fracture area is defined as the sum of fracture areas within the mudstone and sandstone layers. The effective fracture area refers to fracture area contained within the sandstone layer. The effective fracture area ratio is then calculated as the proportion of the effective fracture area relative to the total fracture area. Fig. 7(a) shows that the CLFDP reaches a breakdown pressure of 50.89 MPa, with extension pressures remaining stable at an average of 36.74 MPa. From Fig. 7(b), there is a clear upward trend in the total fracture area over time. Especially, during the period of

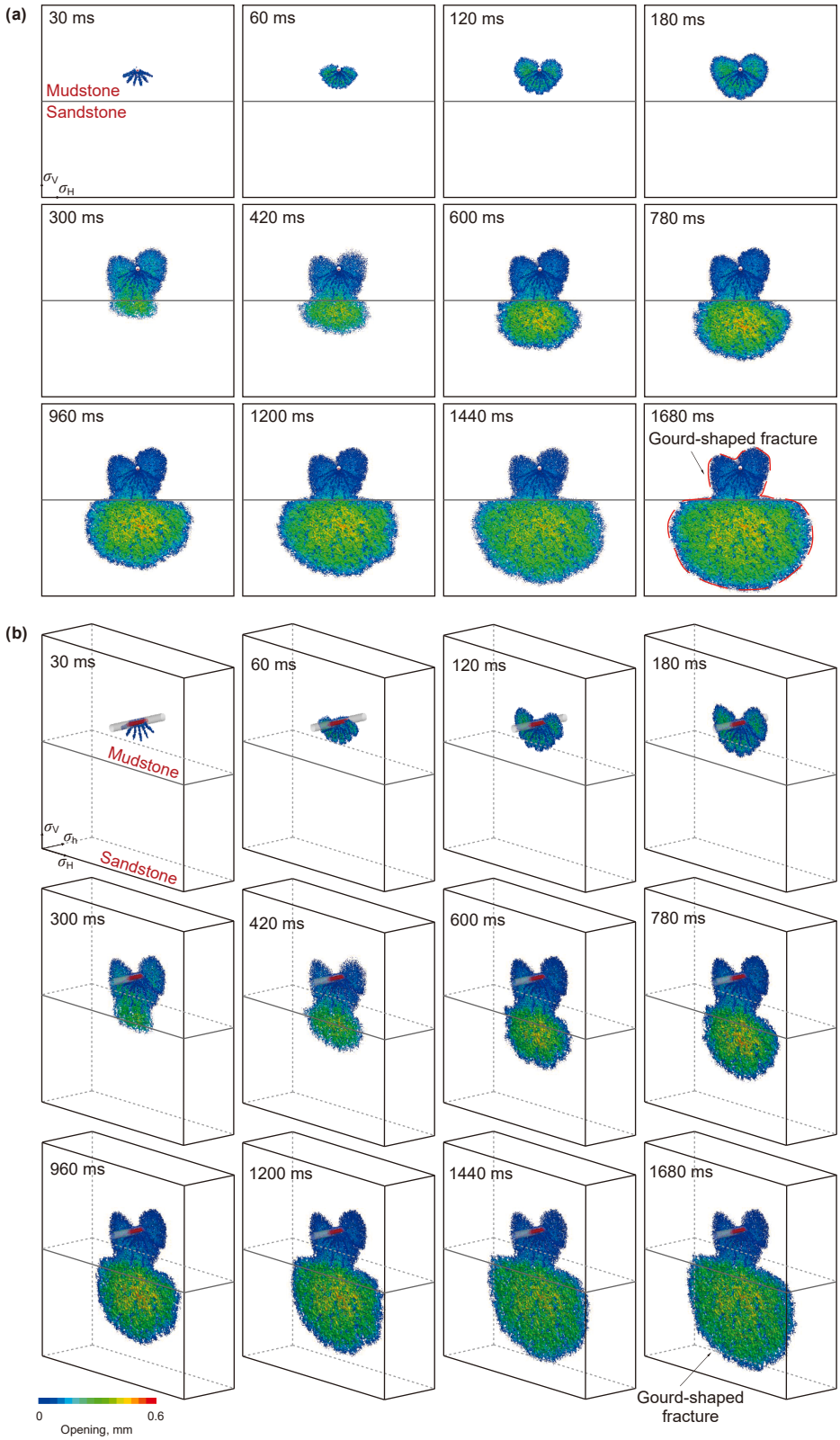


**Fig. 6.** Fracture morphologies of CLFDP evolving with varying injection durations. (**a**) Front view, and (**b**) perspective view.

0–220.80 ms, the effective fracture area remains at zero, suggesting the absence of any effective fractures. This phenomenon occurs because fracture growth remains confined to the mudstone layer, and have not yet broken through into the sandstone reservoir. After 220.80 ms, the effective fracture area begins to rise over time, exhibiting a growth slope nearly equal to that of the total fracture area and the increase magnitude between the two is almost the same. It indicates that during this stage, hydraulic fractures

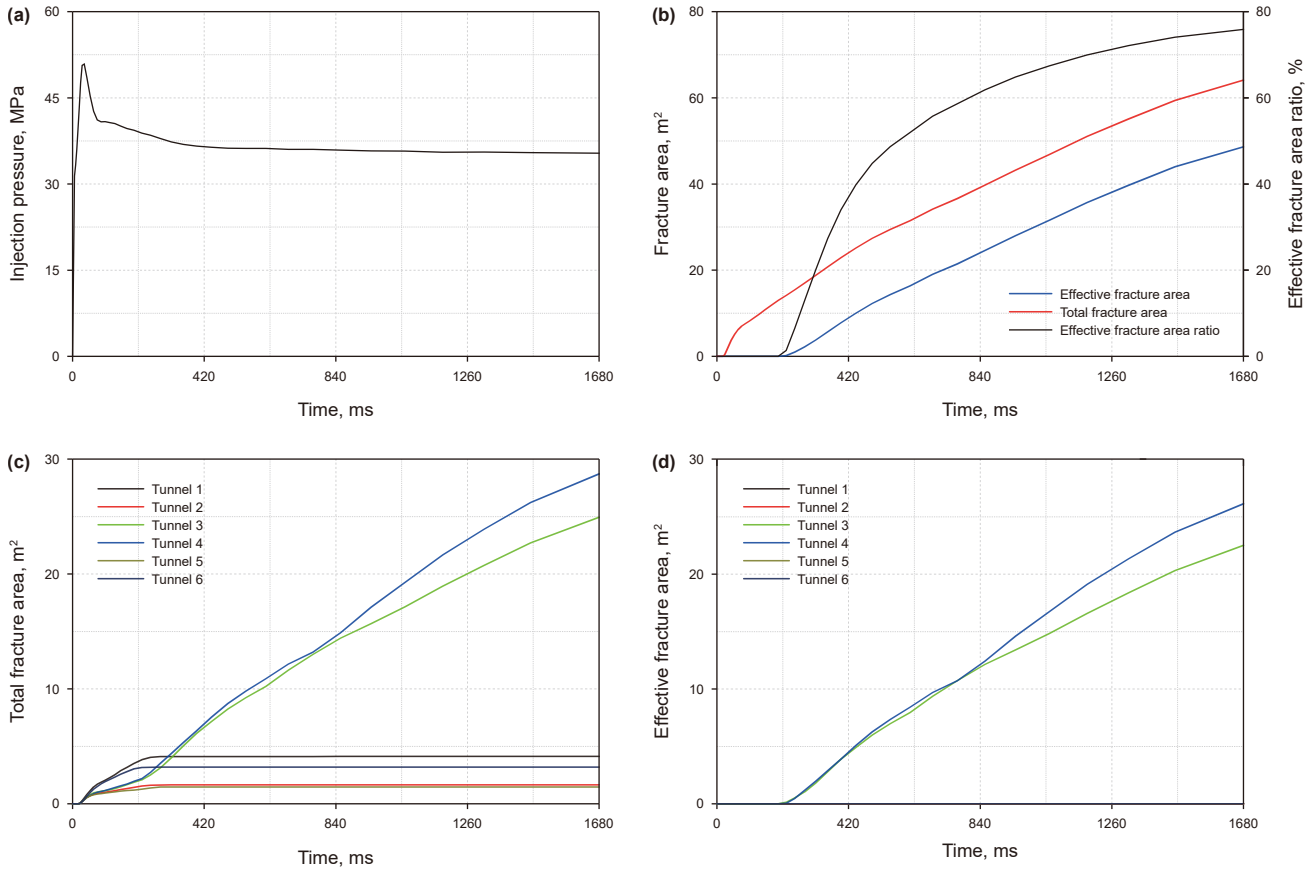


**Fig. 7.** Evolution of (**a**) the injection pressures, (**b**) the total fracture area, effective area, and effective fracture area ratio for the entire model, (**c**) the total fracture area for individual tunnels, and (**d**) the effective fracture area for individual tunnels.

propagate almost exclusively in the sandstone layer, and this observation aligns well with the phenomenon illustrated in Fig. 6. Additionally, the effective fracture area grows faster initially but slows considerably in later stages. During the initial stage (0–220.80 ms), multiple fractures initiate simultaneously from perforation tunnels in the mudstone layer, but the propagation degrees vary as evidenced by differences in their corresponding fracture areas (Fig. 7(c) and (d)). Upon penetrating the lower sandstone layer at 220.80 ms, hydraulic fractures exhibit a preferential propagation in this layer. Consequently, tunnels 3 and 4, closer to the lower sandstone layer, emerge as the dominant pathways.

## 4. Parameter analysis

Building upon the numerical model for CLFDP delineated in Section 3.1, an investigation is conducted to assess the impact of various factors—including the horizontal wellbore position, perforation depth, and perforation spacing—on fracture propagation. This is achieved by systematically altering each factor in isolation. The objective is to furnish theoretical insights that can inform the optimal design of CLFDP.

### 4.1. Effect of horizontal wellbore position

The horizontal wellbore position denotes the vertical distance of the horizontal wellbore in relation to the stratigraphic interface. To elaborate, when the horizontal wellbore is situated beneath the stratigraphic interface—that is, within the confines of the lower sandstone layer—its position is assigned a negative value. When the horizontal wellbore is positioned at the formation interface, its location is defined as 0.0 m. If the wellbore is located above the formation interface (i.e., within the upper mudstone layer), its position is assigned a positive value. The horizontal wellbore position is set within the range of −1.0 to 2.5 m. This selection is based on consideration of research objectives and preliminary simulation results. The lower limit of −1.0 m is chosen to ensure that the wellbore remains entirely within the sandstone layer, while also allowing investigation of fracture cross-layer behavior as hydraulic fractures extend from sandstone into mudstone. Preliminary studies indicate that when the wellbore is positioned at or below −1.0 m, hydraulic fractures primarily propagate within the sandstone layer, exhibiting a relatively consistent, approximately rectangular geometry. Under these conditions, the wellbore position has relatively little influence on the outcome. In addition, when the wellbore position is positive (i.e., within the mudstone layer), its position significantly affects the stimulation results. To investigate this phenomenon, we aim to include as many relevant case scenarios as possible. Therefore, the upper limit is set to the maximum value (2.5 m). Noted that 3.0 m is excluded from the analysis as the wellbore is at the model boundary.

Fig. 8 illustrates that the fracture geometry exhibits diverse forms with various horizontal wellbore position. Specifically, when the wellbore position is at −1.0 m, the fracture manifests a rectangular shape; at −0.5 m, it transitions to a semi-circular; at 0.5 m, it appears a pitcher with a pointed base; and at 1.0 m, it forms a gourd-like shape. It is observed that when the wellbore

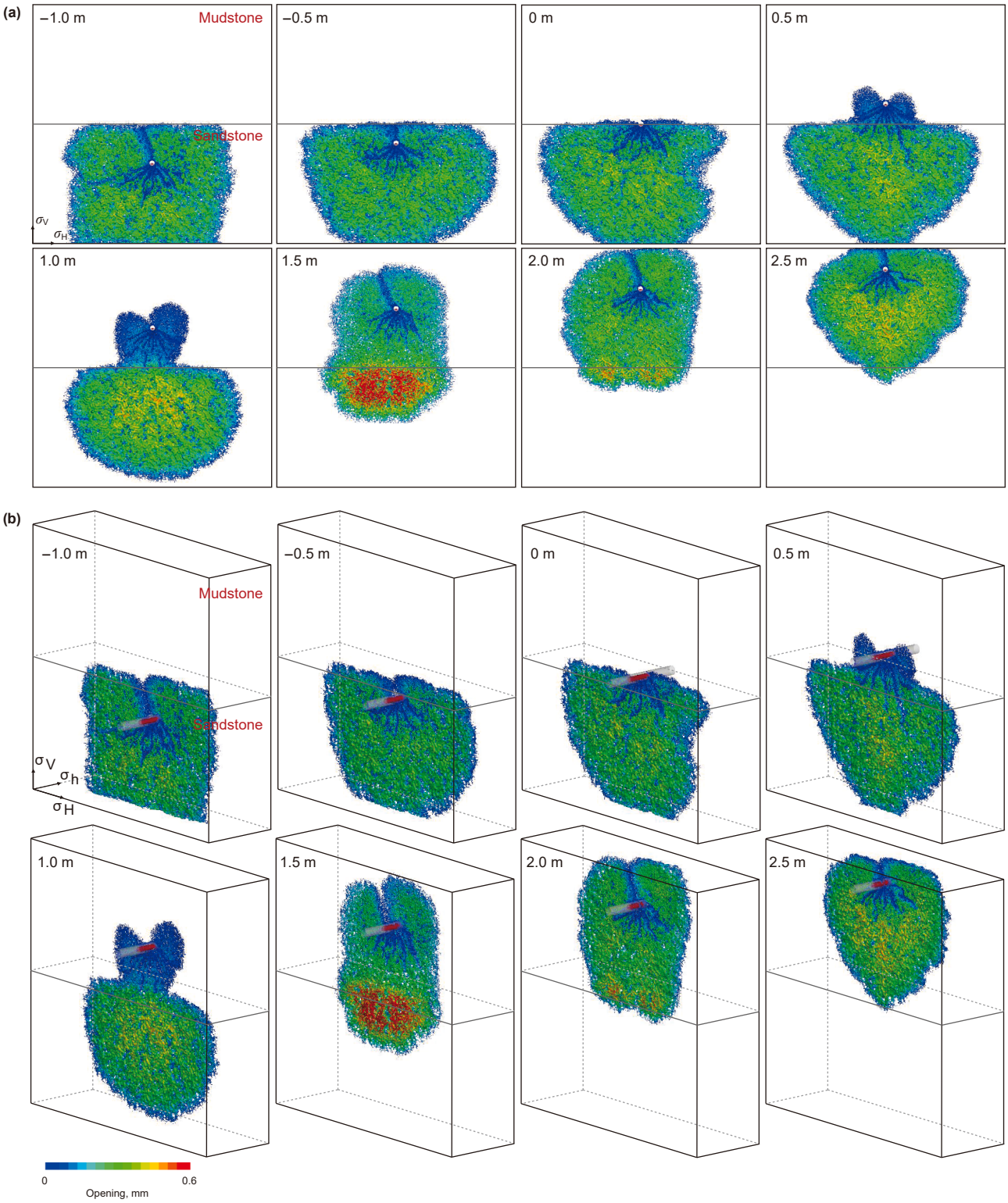


**Fig. 8.** Fracture morphologies for CLFDP under various horizontal wellbore positions. (**a**) Front view, and (**b**) perspective view.

position is at or below 0.0 m, the perforation tunnels are all situated in the sandstone layer. Consequently, hydraulic fractures initiate and propagate predominantly within the sandstone layer from the outset, with negligible penetration into the mudstone layer. As a result, the effective fracture areas for the three scenarios (−1.0, −0.5 and 0.0 m) depicted in Fig. 9 exhibit remarkable similarity. When the horizontal wellbore is positioned at offsets of 0.5 and 1.0 m from the interface, hydraulic fractures initially originate from perforation tunnels located within the mudstone layer. However, owing to the close proximity of tunnels 3 and 4 to the lower sandstone reservoir, the fractures rapidly propagate into the sandstone layer. Subsequently, fracture propagation becomes

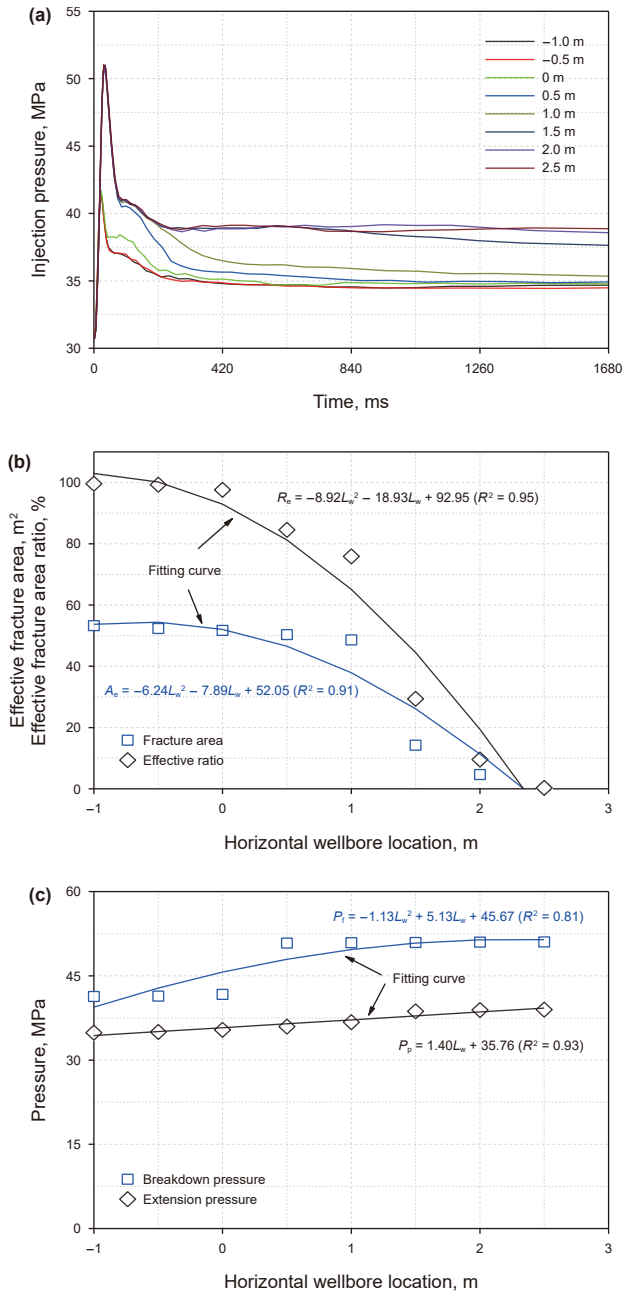


**Fig. 9.** Evolution of (**a**) injection pressure, (**b**) effective fracture area and its ratio, and (**c**) breakdown pressure and average extension pressure under various horizontal wellbore positions.

predominantly confined to the sandstone layer. Moreover, as the wellbore is progressively positioned higher, ascending from 1.5 to 2.5 m—moving it farther from the sandstone layer—hydraulic fractures are compelled to propagate extensively in the mudstone before they can breach the layer and extend into the lower sandstone layer. Consequently, it leads to a diminished efficacy of hydraulic fracturing treatment in the sandstone layer.

In addition, regarding the concern that fracture extension to the boundary may affect the validity of the results, we conduct an analysis and believe that this phenomenon does not compromise the validity of the study's conclusions. The reasons are as follows: (a) The purpose of this section is to examine how the horizontal wellbore position relative to the mudstone-sandstone interface affects the fracture propagation across layers. As illustrated in Fig. 8, when the wellbore is located within the mudstone layer (i.e., horizontal well position $\geq$ 0 m), fracture growth is constrained in the mudstone but extends widely within the sandstone, forming a characteristic "gourd-shaped" structure, a key observation of this study. When the wellbore is situated in the sandstone layer, fractures tend to remain confined within the sandstone and rarely penetrate into the upper mudstone, even when some fractures reach the model boundary. The above behaviors and their qualitative trends are governed primarily by in-situ stresses and lithological contrasts, and the underlying physical mechanisms are established before fractures reach the boundary. (b) From the injection pressure curve shown in Fig. 9(a), even in cases where fractures extend to the boundary, the pressure curve remains smooth and continuous in the later stages, with no pressure anomalies or abrupt changes caused by boundary effects. This indicates that the fracture propagation is generally stable, and that boundary conditions have limited influence on the qualitative judgment of the simulation results, thereby supporting the validity of simulation results. Of course, we fully acknowledge that fracture extension to the model boundary may indeed influence quantitative analysis. Therefore, we plan to further increase the model size in future studies, and explore the advanced techniques such as GPU parallel computing to enhance computational efficiency. This endeavor aims to more accurately capture the dynamic propagation of fractures in the CLFDP.

There is, on the whole, a noticeable trend where the breakdown pressure exhibits an increase in tandem with the rising wellbore position (Fig. 9(a) and (c)). In all cases where the wellbore position is $\leq$ 0.0 m, the breakdown pressure remains consistently around 41.0 MPa—significantly lower than that observed in cases where the wellbore position is $\geq$ 0.5 m (approximately 51.0 MPa). This discrepancy arises from the differing lithologies at the perforation sites. In the former scenario, perforations are situated within the sandstone layer, where hydraulic fractures initiate at a relatively low breakdown pressure. Conversely, in the latter scenario, perforations were placed in the mudstone layer, requiring greater breakdown pressure for fracture propagation. Similarly, the extension pressure exhibits a comparable trend of change. Concurrently, the correlations between the breakdown pressure $P_f$ and the average extension pressure $P_p$ with respect to the wellbore position $L_w$ are mathematically fitted. The breakdown pressure is represented by $P_f = -1.13L_w^2 + 5.13L_w + 45.67$ $\left(R^2 = 0.81\right)$, while the average extension pressure follows the equation $P_p = 1.40L_w + 35.76$ $\left(R^2 = 0.93\right)$. One of the core tasks in on-site fracturing design is to predict the construction pressure window (including breakdown pressure and extension pressure), based on geological and engineering conditions. Our fitting model effectively establishes a predictive tool with wellbore position as input and key injection pressure as output. In practical applications, once the wellbore position is determined through downhole measurements, the model can estimate the required injection pressure for the operation. This provides a basis for setting fracturing pump units, optimizing pump schedules, and mitigating operational risks. Therefore, the established mathematical correlations align closely with on-site engineering requirements and hold strong potential for on-site operations.

Furthermore, Fig. 9(b) demonstrates that both the effective fracture area and its ratio decrease monotonically as the wellbore position increases. Notably, when the wellbore position rises from −1.0 to 0.0 m, the reduction in the above parameters is marginal. Specifically, the effective fracture area exhibits a decline, dropping from 53.27 to 51.71 $m^2$, and the effective fracture area ratio follows suit, decreasing from 99.61% to 97.62%. However, a more pronounced reduction is observed when the wellbore position is adjusted from 1.0 to 1.5 m. In this scenario, the effective

fracture area plummets from 48.64 to a mere 14.27 $m^2$, while the effective fracture area ratio experiences a substantial drop, from 75.89% down to 29.36%. This finding demonstrates that the wellbore position of 1.0 m represents a critical threshold. It is noted that deriving a threshold solely from these eight discrete cases is not entirely rigorous, since the value of 1.0 m represents the optimum only within the above scenarios. If additional simulations are performed with finer intervals, such as at 0.9, and 1.1 m, the optimal position might deviate slightly. Furthermore, when the horizontal wellbore exceeds this value, a significant deterioration in fracturing performance is observed. It is therefore imperative to account for this factor in the selection of optimal wellbore sections for fracturing. The aforementioned analysis underscores that horizontal wellbore should be optimally steered to ensure maximum penetration through the target reservoir, such as using the rotary steering technology (Andrade et al., 2021; Chen et al., 2023, 2024; Gao, 2022; Zafarian et al., 2021). By doing so, it yields a substantial reduction in injection pressure during hydraulic fracturing and an increase of both the effective fracture area and its ratio, ultimately culminating in superior stimulation effects. Moreover, we derived quantitative fitting formulas describing the relationship between both the effective crack area $A_e$ and its ratio $R_e$ with respect to wellbore position $L_w$ as follows: $A_e = -6.24{L_w}^2 - 7.89L_w + 52.05$ $\left(R^2 = 0.91\right)$, and $R_e = -8.92{L_w}^2 - 18.93L_w + 92.95$ $\left(R^2 = 0.95\right)$.

### 4.2. Effect of perforation depth

Fig. 10 illustrates fracture morphologies for CLFDP under various perforation depths. Obviously, as the perforation depth escalates, fracture propagation in the upper mudstone layer exhibits a progressively diminishing range. Conversely, fracture propagation in the lower sandstone layer attains a continuous increment. Specifically, when perforation depth is 0.5 or 1.0 m, perforation tunnels are confined to the mudstone layer, and hydraulic fractures must firstly initiate and propagate in the mudstone layer before extending into the adjacent sandstone reservoir. Consequently, a significant portion of hydraulic fractures remains in the mudstone layer. When perforation depth ranges from 1.50 to 2.50 m, certain perforation tunnels are situated in the sandstone layer, resulting in hydraulic fractures almost only starting and expanding from the segments of perforation tunnels located in the sandstone reservoir. In contrast, the segments of perforation tunnels located in mudstone layer encounter challenges in effectively initiating fractures. As a result, transverse main fractures that efficiently transform sandstone reservoir are formed.

Both the breakdown pressure and average extension pressure decrease with the increase of perforation depth (Fig. 11(a) and (c)). Specifically, when perforation depth increases from 0.5 to 2.5 m, the breakdown pressure abates from 50.89 to 43.71 MPa, with a

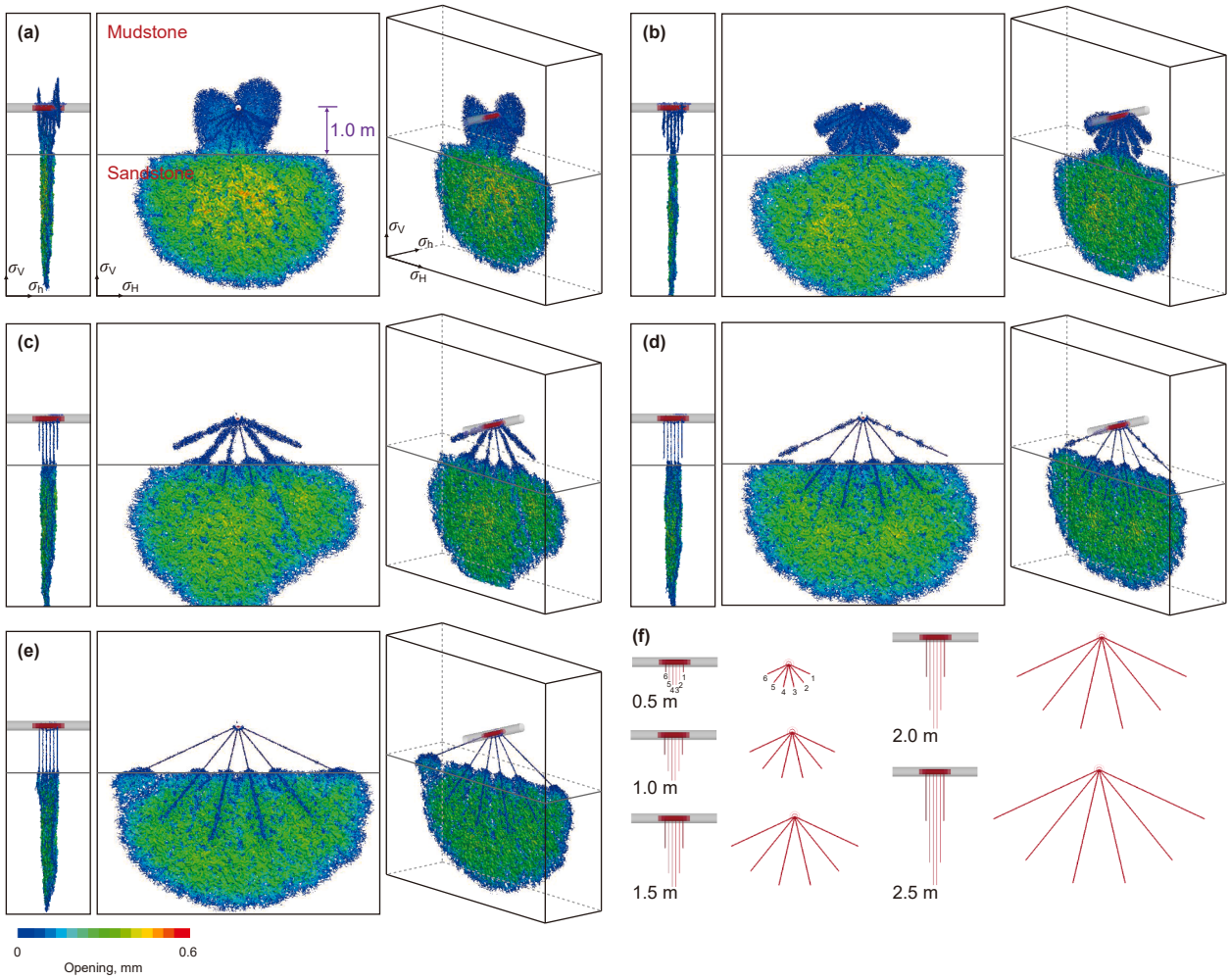


**Fig. 10.** Fracture morphologies for CLFDP under various perforation depths. (**a**) 0.5 m, (**b**) 1.0 m, (**c**) 1.5 m, (**d**) 2.0 m, (**e**) 2.5 m, and (**f**) schematic diagram of different perforation depths.

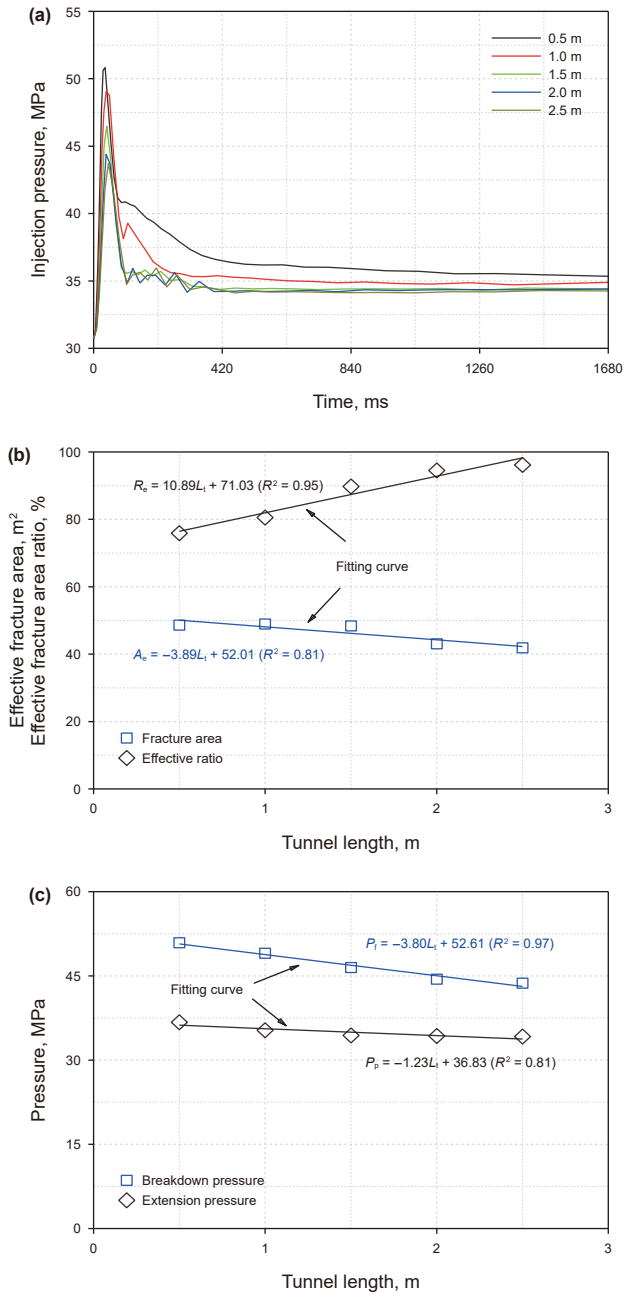


**Fig. 11.** Evolution of (**a**) injection pressure, (**b**) effective fracture area and its ratio, and (**c**) breakdown pressure and average extension pressure under various perforation depths.

decrease of 14.11%. The average extension pressure reduces from 36.74 to 34.18 MPa, corresponding to a 6.97% reduction. Furthermore, a quantitative analysis is conducted to establish the relationships between the breakdown pressure $P_f$ and the average extension pressure $P_p$ with the variation of perforation depth $L_t$. The resulting fitted equations are as follows: $P_f = -3.80L_t + 52.61$ $\left(R^2 = 0.97\right)$, and $P_p = -1.23L_t + 36.83$ $\left(R^2 = 0.81\right)$. The effective fracture area ratio displays a significant growth from 75.89% to 96.13% with increasing perforation depth (Fig. 11(b)). The relationships between the perforation depth $L_t$ and both the effective fracture area $A_e$ and its ratio $R_e$ are derived through linear regression. The fitted equations are as follows: $A_e = -3.89L_t + 52.01$ $\left(R^2 = 0.81\right)$, and $R_e = 10.89L_t + 71.03$ $\left(R^2 = 0.95\right)$.

Drawing from the preceding analysis, it becomes evident that when horizontal wellbores stray from the target sandstone reservoir, the deep-penetration perforation technology (Cai et al., 2024; Fu et al., 2025; Gensheng et al., 2007) should be deployed. This technology can promote extensive propagation of hydraulic fractures within the target reservoir. It also significantly reduces the injection pressure, including the breakdown pressure and extension pressure. Together, these effects achieve effective stimulation of NRHWI. This method shatters the long-standing constraint in traditional fracturing design that NRHWI is discouraged as the fracturing interval candidates.

### 4.3. Effect of perforation spacing

The perforation spacing denotes the distance separating two adjoining perforation tunnels. Fig. 12 proves that rising the perforation spacing inhibits multiple-tunnel fractures communication and coalescence after initiation. The propagation of individual-tunnel fracture becomes more independent, eventually leading to the development of branching fractures near the wellbore and, in some cases, the formation of multiple primary fractures (Fig. 12(g)). Specifically, when perforation spacing is 30.48–76.20 mm, hydraulic fractures initiating from multiple tunnels merge and develop into continuous, smooth main fractures in the vicinity of the wellbore. As perforation spacing raises from 91.44 to 182.88 mm, fractures starting from certain tunnels gradually lost connectivity with adjacent fractures. This is particularly evident for fractures originating from the outermost two tunnels, which develop into independent branching fractures. When perforation spacing widens to 243.84 mm, there is no interconnection observed between all fractures initiating from tunnels, and instead these fractures propagate autonomously. Notably, during this independent propagation, a fierce competitive dynamic emerges, resulting in only a limited number of fractures becoming the predominant main fractures, as exemplified by fractures initiating from tunnels 3 and 5.

From Fig. 13(a) and (c), the perforation spacing has minimal influence on injection pressure. With rising perforation spacing, the breakdown pressure fluctuates within a narrow range of 50.89–51.50 MPa, confirming a variation amplitude of merely 0.61 MPa. Similarly, the average extension pressure varies slightly from 36.42 to 37.90 MPa, with a limited fluctuation range of only 1.48 MPa. More importantly, an observed phenomenon is that increasing perforation spacing prolongs the time required for injection pressure to reach breakdown pressure. This occurs because, at smaller perforation spacings, fractures initiating from adjacent tunnels tend to propagate and coalesce earlier, facilitating the rapid creation of a dominant fracture and thus an earlier attainment of breakdown pressure. Conversely, when perforation spacing is excessively large, fractures emanating from tunnels exhibit delayed or insufficient communication, impeding their coalescence. Under such conditions, the development of a dominant fracture relies primarily on the extensive propagation of fracture from an isolated tunnel, necessitating a longer duration to achieve breakdown pressure.

As depicted in Fig. 13(b), both the effective fracture area $A_e$ and its ratio $R_e$ show a pattern of initial decline followed by a subsequent rise as perforation spacing $D_t$ increases. The corresponding fitting formulas are: $A_e = 0.0009{D_t}^2 - 0.2644D_t + 58.9050$ $\left(R^2 = 0.78\right)$, and $R_e = 0.0010{D_t}^2 - 0.3464D_t + 92.1080$ $\left(R^2 = 0.91\right)$. More precisely, as perforation spacing expands from 30.84 to 182.88 mm, the effective fracture area diminishes from 50.40 to 36.07 $m^2$, marking a reduction of 28.43% (equivalent to 14.33 $m^2$). Concurrently, the effective fracture area ratio declines from 80.29% to 57.91%. Additionally, reducing perforation spacing from 243.84

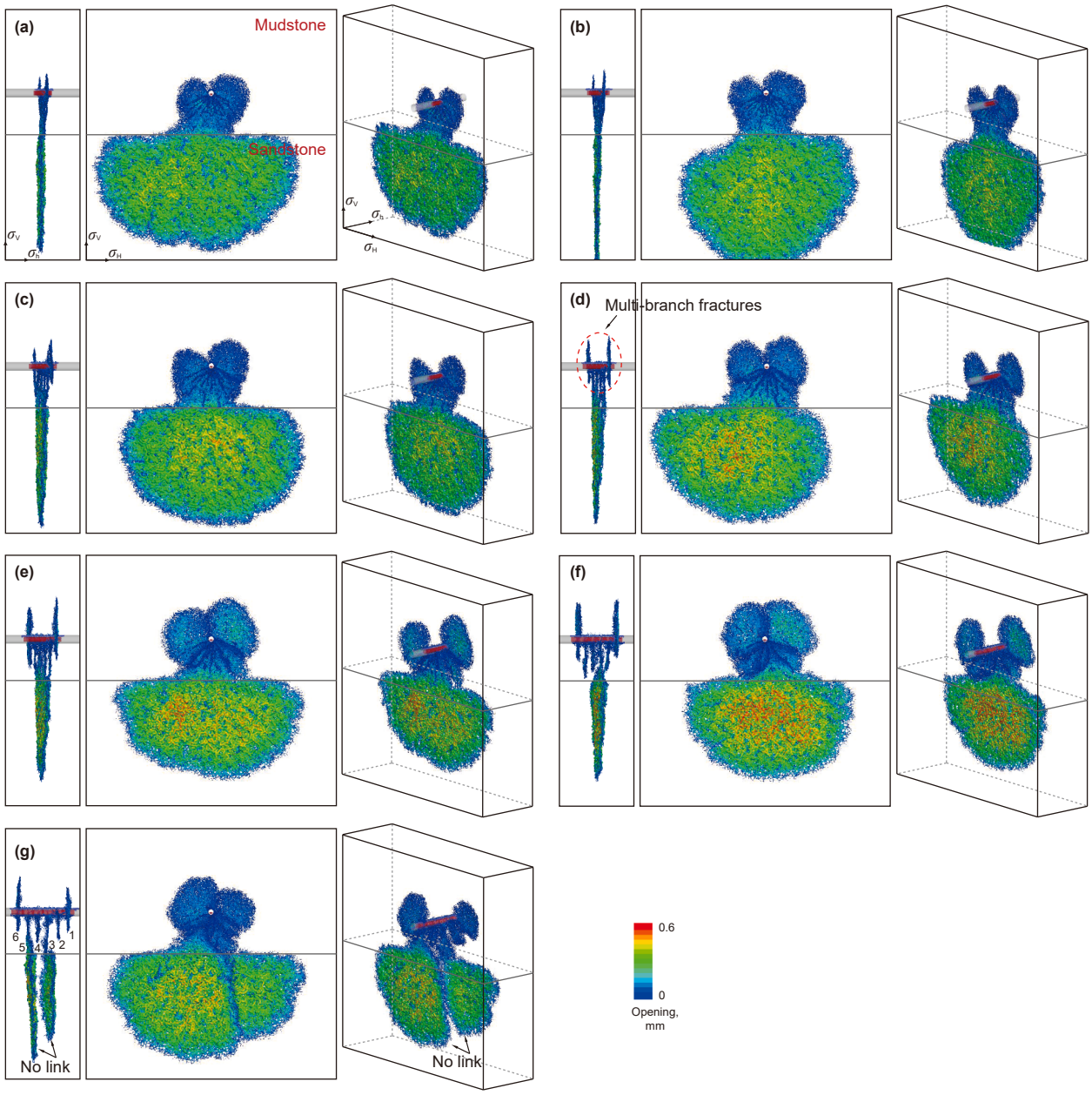


**Fig. 12.** Fracture morphologies for CLFDP under various perforation spacings. (**a**) 30.48 mm, (**b**) 45.72 mm, (**c**) 76.20 mm, (**d**) 91.44 mm, (**e**) 121.92 mm, (**f**) 182.88 mm, and (**g**) 243.84 mm.

to 182.88 mm enhances stimulation effectiveness, as evidenced by the decrease in effective fracture area (46.55–36.07 $m^2$) and fracture area ratio (65.74%–57.91%). In conclusion, higher perforation density is the primary determinant for superior stimulation results. Consequently, field operations should prioritize configurations with minimized perforation spacing.

## 5. Discussion

This paper develops a three-dimensional numerical model for CLFDP, explicitly accounting for the presence of actual perforation tunnels. This work offers a research method for further systematically investigating the effects of perforation parameters—including perforation diameter, phase angle, and perforation number—on hydraulic fracture propagation in the future. In this study, we did not explore the effect of phase angle, primarily because its influence is also related to the in-situ stresses, which is a complex coupling effect. Specifically, when the phase angle changes, the orientation of each perforation tunnel relative to the principal stress directions also varies, which significantly affects the fracture initiation and propagation behavior of each perforation tunnel. And this interaction may not exhibit a regular trend with varying phase angles. Therefore, the role of phase angle constitutes a more complex and nuanced topic, warranting extensive analysis and discussion in future work. Building on the current study, we plan to systematically investigate the influence of phase angle under various configurations, such as single and multiple perforation tunnels. We consider this a highly promising direction for future research.

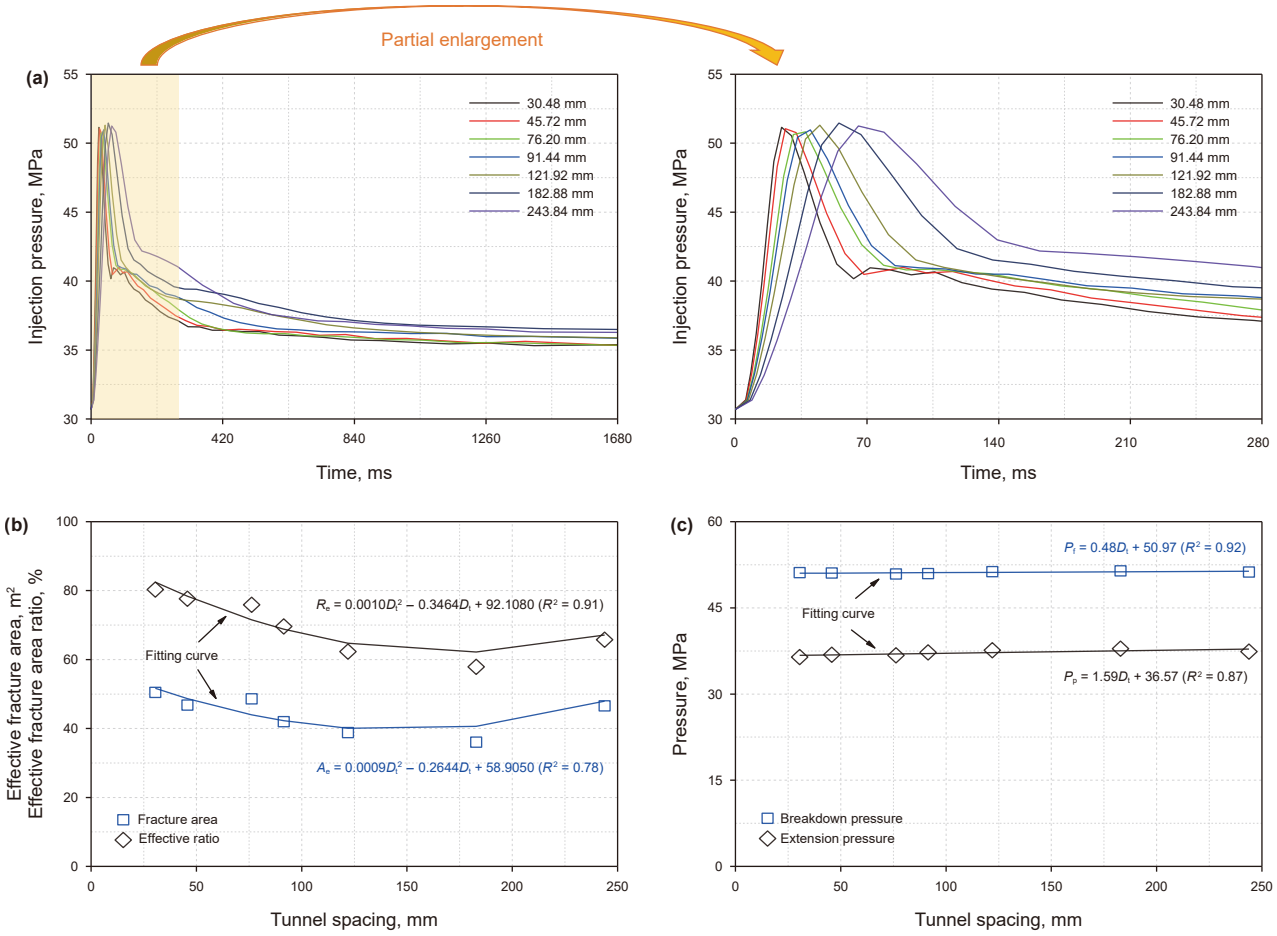


**Fig. 13.** Evolution of (**a**) injection pressure, (**b**) effective fracture area and its ratio, and (**c**) breakdown pressure and average extension pressure under various perforation spacings.

(1) Discussion on stress shadow effect and influence of in-situ stress

Stress shadow effect: In our simulation results, the stress shadow effect is primarily manifested in the interaction among multiple fractures. When the perforation spacing is small (e.g., 30.48–76.20 mm), fractures originating from adjacent perforation tunnels rapidly propagate and interfere with one another. The resulting stress shadow effect inhibits the further extension of certain fractures, particularly those initiating in mudstone layers. This phenomenon promotes energy and fluid toward more favorable fractures leading into sandstone layers. It accelerates the formation of a dominant fracture and enhances its propagation within sandstone reservoirs. Conversely, with larger perforation spacing (e.g., 243.84 mm), the stress shadow effect diminishes, allowing fractures originating from adjacent tunnels to propagate more independently. This leads to intensified competition among multiple fractures, with only a few overcoming the constraints imposed by the stress field and rock mechanical properties to become dominant fractures (as illustrated in Fig. 12). These observations explain why high-density perforation (i.e., small spacing) tends to form more continuous and effective main fractures, whereas larger spacing is more likely to result in branching or multiple competing fractures, thereby reducing stimulation efficiency.

Influence of in-situ stress: The simulation results indicate that, regardless of the wellbore's position within the mudstone layer, hydraulic fractures exhibit a strong tendency to deflect and extend toward the underlying sandstone reservoir after initiation. This behavior is largely governed by the in-situ stress field, which directs fracture propagation. In the present cases, the lower sandstone reservoir offers a more mechanically favorable environment for fracture growth compared to the upper mudstone layer, exemplified by a lower minimum horizontal principal stress. Consequently, whenever conditions permit (e.g., through sufficiently deep perforations or proximity to the lithological interface), fractures preferentially and extensively propagate within the sandstone layers.

(2) Discussion on the threshold of critical wellbore position

Our analysis reveals that, as the wellbore position is increased from 0.0 to 1.0 m, the effective fracture area ratio begins to decline significantly and monotonically (Fig. 9). When the wellbore position is > 1.0 m, stimulation performance in the sandstone reservoir deteriorates sharply, as fractures must traverse a greater distance through the overlying mudstone, leading to higher energy dissipation before reaching the target zone. Therefore, a critical threshold of 1.0 m is identified for achieving effective enhancement. In fact, this critical threshold is not only influenced significantly by perforation parameters but is also closely tied to the in-situ stress. On one hand, as displayed in Fig. 10, increasing the perforation depth can effectively compensate for the unfavorable wellbore position. For instance, even when the wellbore position lies above the threshold (i.e., at 1.0 m), deep-penetration perforations (e.g., with a perforation depth of 1.5–2.5 m) can extend the

perforation tunnel into or near the sandstone reservoir. This bypasses the unfavorable mudstone interval, either enabling direct fracture initiation in the sandstone or significantly shortening the fracture path to the target layer. This mechanism allows the operable "critical wellbore position threshold" to be effectively raised through optimized perforation design, offering a practical remedial strategy for cases where wellbore trajectory control is less than ideal. On the other hand, the critical wellbore position threshold arises from the interplay between perforation geometry, and the in-situ stress. It marks the point beyond which the natural turning capacity of hydraulic fractures driven solely by in-situ stresses becomes inadequate to overcome the barrier effect of the mudstone layer. Beyond this threshold, proactive intervention, such as deep-penetration perforation, becomes necessary.

The current numerical modeling still presents certain limitations that warrant further refinement. Firstly, an important factor, the influence of proppants, is overlooked. During hydraulic fracturing, fracturing fluid contains a substantial number of solid particles (i.e., proppants). These particles serve a critical purpose: they are deposited within the fractures to prop them open, thereby preventing full closure. Consequently, fluid flow in the fracturing system constitutes a solid-liquid two-phase flow, as evidenced by several researches (Dontsov, 2023; Patel et al., 2024; Wang J. et al., 2023; Zhang B. et al., 2025a; Zhang et al., 2023; Zhou et al., 2025; Gu et al., 2025). This stands in contrast to the single-phase flow assumption made in this paper. The propagation of hydraulic fractures, propelled by a two-phase fluid, displays a far more intricate behavior. However, this complexity brings it closer to real-world scenarios. For this reason, we are attempting to simulate hydraulic fracturing driven by multiphase fluids. In these simulations, the fluid flow is computed utilizing OpenFoam, a pivotal task of significant value.

Furthermore, this study does not account for the presence of compacted damage zones surrounding perforation tunnels. In reality, perforation process—particularly when employing shaped-charge perforating guns (also referred to as explosive perforation)—induces significant rock deformation, breakage, and compaction in the vicinity of the tunnels. This results in the occurrence of a compacted damage zone, which typically comprises a crushing region and a low-permeability region (Arora and Sharma, 2000; Craddock et al., 2018; Liang et al., 2023; Pucknell and Behrmann, 1991; Yan et al., 2020). The existence of compacted damage zones significantly affects the flow dynamics of fracturing fluid and the initiation behaviors of fractures. To date, relatively few studies have succeeded in incorporating the effects of these compaction damage zones, with the predominant methodology being confined to indoor experiments. There is still a significant gap in numerical simulation, primarily stemming from the challenges associated with incorporating the presence of perforation tunnels in the existing numerical methods. The modeling method proposed in this study consider the presence of perforation tunnels, thereby offering a viable approach to explore the impact of compacted damage zones on fracture initiation and propagation. Therefore, we will define the surrounding strata of perforation tunnels as the compaction damage zone locally in the next step on basis of the numerical model in this paper. The relevant parameters of this zone will be calibrated based on laboratory test results to systematically examine the influence of the compaction damage zone. This direction of research holds significant promise for further exploration.

Thirdly, field observations demonstrate that non-uniform dimensions of perforation tunnels even in the same cluster occur, due to the eccentricity and gravity effects of perforation gun (Almaguer et al., 2002). This study, however, assumes an idealized scenario with identical tunnel sizes, which represents a simplification of real-world conditions. Given that the dimensions of each tunnel vary, the resulting perforation friction differs. This discrepancy subsequently influences the fluid distribution among these tunnels, and consequently impacts the propagation of hydraulic fractures. Accounting for the non-uniform tunnel sizes will facilitate the optimization of both perforation dimensions and spatial configuration under varying operational scenarios. This includes scenarios where horizontal wellbores are positioned in either the upper or lower interlayers. Such optimization is crucial for achieving optimal stimulation outcomes.

Fourthly, in the current model, the leak-off effect (such as Carter leak-off) and non-Newtonian fluid behavior have not been incorporated, mainly for the following reasons: (i) The research focus lies in providing an option for simulating the CLFDP and offering practical engineering recommendations. Therefore, we adopt a simplified modeling framework that avoids interference from multiple complex parameters including the filtration and fluid mechanics behavior. (ii) Incorporating the leak-off effect, particularly pressure-dependent dynamic leak-off, along with the power-law fluid constitutive model would significantly increase the nonlinearity of the governing equations and the difficulty of obtaining solutions. Moreover, it also leads to a substantial rise in computational cost. For instance, the current model, which assumes constant fluid viscosity and no leak-off, contains approximately 1.56 million nodes. When simulated on a workstation equipped with an Intel(R) Core(TM) i9-14900K 3.20 GHz processor, a single model requires about 45 h to complete. Therefore, incorporating the aforementioned fluid features into the model would further escalate the computational demands, potentially to an unbearable extent. In summary, considering the above factors, we have consciously chosen not to include the leak-off model and non-Newtonian fluid relationship in the current model, which is a necessary compromise under the present conditions. Of course, we also acknowledge the significance of studying the effects of fluid leak-off and non-Newtonian behavior on fracture propagation (Moukhtari and Lecampion, 2018; Pereira and Lecampion, 2021). This is a highly valuable and necessary direction for our subsequent research and also serves as a natural extension of the current work.

## 6. Conclusions

This study develops a 3D numerical model for CLFDP, systematically discussing the impact of horizontal wellbore position, perforation depth, and perforation spacing. The primary findings are outlined as follows:

(1) In the case study where the horizontal wellbore is situated within the upper mudstone layer overlying the sandstone reservoir, a distinctive gourd-shaped fracture emerges. This fracture exhibits limited propagation in the mudstone layer but extends extensively into the underlying sandstone reservoir. Besides, the breakdown pressure and average extension pressure are measured at 50.89 and 36.74 MPa, respectively, while the effective fracture area ratio reaches an impressive 75.89%.

(2) When the wellbore position transitions from the sandstone layer to the upper mudstone layer, both the breakdown pressure and extension pressure generally exhibit a gradual escalation. Conversely, the effective fracture area and its corresponding ratio show a monotonic decline. The study identifies a critical wellbore position threshold to achieve the optimal stimulation. Therefore, the horizontal wellbore should be precisely steered to ensure maximum penetration through the target reservoir, such as using the rotary

steering technology, which serves as a key measure for enhancing stimulation efficiency.

(3) As the perforation depth lengthens, hydraulic fracture propagation exhibits contrasting trends between geological layers: while it progressively decreases in the upper mudstone formation, it shows significant enhancement in the lower sandstone reservoir. This differential propagation behavior results in a remarkable improvement in the effective fracture area ratio, which increases substantially from 75.89% to 96.13%. Concurrently, both the breakdown pressure and average extension pressure demonstrate a decreasing trend with greater perforation depth. These findings suggest that for horizontal wellbores deviating from the target sandstone reservoir, deep-penetration perforation represents an optimal strategy for effectively stimulating the NRHWI.

(4) Rising perforation spacing promotes the independent propagation of fractures emanating from individual perforation tunnels while inhibits fracture coalescence. This mechanism ultimately results in branched fractures near the wellbore and, in certain instances, the emergence of multiple primary fractures. Notably, observations reveal that the perforation spacing exhibits negligible impact on both breakdown pressure and extension pressure. The effective fracture area and its corresponding ratio initially decrease before increasing as perforation spacing expands. These findings collectively suggest that optimal operation strategies should employ reduced perforation spacing configurations (i.e., higher perforation density) to maximize stimulation effectiveness.

## CRediT authorship contribution statement

**Xiao-Hua Wang:** Writing – original draft, Investigation, Formal analysis, Data curation. **Liu-Ke Huang:** Writing – review & editing, Validation, Supervision, Investigation, Funding acquisition, Formal analysis, Data curation, Conceptualization. **Chang-Heng Li:** Investigation, Formal analysis, Data curation. **An-An Wu:** Validation, Investigation, Formal analysis. **Sheng-Rong Zhu:** Writing – original draft, Investigation, Formal analysis. **Li Qian:** Investigation, Formal analysis, Data curation. **Kuan Lu:** Formal analysis, Data curation.

## Data availability

Data will be made available upon reasonable request.

## Declaration of competing interest

The authors declare that they have no known competing financial interests or personal relationships that could have appeared to influence the work reported in this paper.

## Acknowledgements

The authors acknowledge the support provided by the National Natural Science Foundation of China (No. 42407223, and No. 42372337), Shanghai Pujiang Program (No. 24PJD119), Postdoctoral Fellowship Program of CPSF (No. GZB20240557), and Natural Science Starting Project of SWPU (No. 2022QHZ009).

## References

Almaguer, J., Manrique, J., Saliya, W., et al., 2002. Orienting perforations in the right direction. Oilfield Rev. 14, 16–31. https://perforators.org/wp-content/uploads/2017/02/5_Orienting-perforations-in-the-right-direction.pdf.

Andrade, C.P.S., Saavedra, J.L., Tunkiel, A., et al., 2021. Rotary steerable systems: mathematical modeling and their case study. J. Pet. Explor. Prod. Technol. 11, 2743–2761. https://doi.org/10.1007/s13202-021-01182-6.

Arora, D.S., Sharma, M.M., 2000. The nature of the compacted zone around perforation tunnels. In: SPE International Symposium on Formation Damage Control. https://doi.org/10.2118/58720-MS.

Bai, Q., Konietzky, H., Zhang, C., et al., 2021. Directional hydraulic fracturing (DHF) using oriented perforations: the role of micro-crack heterogeneity. Comput. Geotech. 140, 104471. https://doi.org/10.1016/j.compgeo.2021.104471.

Blunt, M.J., Sun, S., Boone, M.A., et al., 2025. Digital rock physics and fluid flow in the context of the energy transition. Adv. Geo-Energy Res. 18, 299–302. https://doi.org/10.46690/ager.2025.12.10.

Cai, S., Yu, Q., Qiao, Y., et al., 2024. Application of the new 102 ultra-deep penetration perforator in the FX-1 well. In: International Field Exploration and Development Conference. https://doi.org/10.1007/978-981-97-0479-8_21.

Chen, J.Q., Wang, K.J., Tang, X.Y., et al., 2024. Steering ability rapid evaluation of the slide drilling system based on multi-body dynamics model. Geoenergy Sci. Eng. 237, 212813. https://doi.org/10.1016/j.geoen.2024.212813.

Chen, M., Jiang, H., Zhang, G.Q., et al., 2010. The experimental investigation of fracture propagation behavior and fracture geometry in hydraulic fracturing through oriented perforations. Petrol. Sci. Technol. 28, 1297–1306. https://doi.org/10.1080/10916466.2010.483435.

Chen, T., Liu, G., He, X., et al., 2023. Calculation method of the build-up rate of the internal push point-the-bit rotary steering tool. Geoenergy Sci. Eng. 230, 212177. https://doi.org/10.1016/j.geoen.2023.212177.

Craddock, G.G., Smith, J., Haggerty, D., 2018. Perforation crushed zone characteristics in a subsurface sandstone. In: SPE International Conference and Exhibition on Formation Damage Control. https://doi.org/10.2118/189483-MS.

Damjanac, B., Cundall, P., 2016. Application of distinct element methods to simulation of hydraulic fracturing in naturally fractured reservoirs. Comput. Geotech. 71, 283–294. https://doi.org/10.1016/j.compgeo.2015.06.007.

Damjanac, B., Detournay, C., Cundall, P., et al., 2011. XSite-description of Formulation. Itasca Consulting Group., Inc.

Damjanac, B., Detournay, C., Cundall, P.A., 2016. Application of particle and lattice codes to simulation of hydraulic fracturing. Comput. Part. Mech. 3, 249–261. https://doi.org/10.1007/s40571-015-0085-0.

Dong, S., Li, R., 2025. Optimization of volume fracturing perforation scheme for horizontal well. Eng. Res. Express 7, 025408. https://doi.org/10.1088/2631-8695/adcb95.

Dontsov, E.V., 2023. A model for proppant dynamics in a perforated wellbore. Int. J. Multiphas. Flow 167, 104552. https://doi.org/10.1016/j.ijmultiphaseflow.2023.104552.

Dontsov, E.V., 2016. An approximate solution for a penny-shaped hydraulic fracture that accounts for fracture toughness, fluid viscosity and leak-off. R. Soc. Open Sci. 3, 160737. https://doi.org/10.1098/rsos.160737.

Fu, Y., Yuan, G., Xia, Y., et al., 2025. Research on improving injection and production gas capacity based on integrated reservoir-well coupling model for gas storage. Fuel 393, 135018. https://doi.org/10.1016/j.fuel.2025.135018.

Gao, D., 2022. Some research advances in well engineering technology for unconventional hydrocarbon. Nat. Gas. Ind. B 9, 41–50. https://doi.org/10.1016/j.ngib.2021.08.016.

Gensheng, L., Zhongwei, H., Jilei, N., et al., 2007. The productivity-enhancing technique of deep penetrating perforation with a high-pressure water jet. Petrol. Sci. Technol. 25, 289–297. https://doi.org/10.1081/LFT-200056824.

Gu, T., Wang, H., Gan, Q., et al., 2025. The impact of forced closure on proppant distribution of hydraulic fracturing in shale formations. Deep Undergr. Sci. Eng. https://doi.org/10.1002/dug2.70065.

He, Q., Zhu, L., Li, Y., et al., 2021. Simulating hydraulic fracture re-orientation in heterogeneous rocks with an improved discrete element method. Rock Mech. Rock Eng. 54, 2859–2879. https://doi.org/10.1007/s00603-021-02422-1.

Huang, L., Deng, L., Wu, A., et al., 2025a. Investigating hydraulic fracture penetration in soft-hard interlayer coal measures with perforated completion. Eng. Fract. Mech. 327, 111467. https://doi.org/10.1016/j.engfracmech.2025.111467.

Huang, L., Dontsov, E., Fu, H., et al., 2022. Hydraulic fracture height growth in layered rocks : perspective from DEM simulation of different propagation regimes. Int. J. Solid Struct. 238, 111395. https://doi.org/10.1016/j.ijsolstr.2021.111395.

Huang, L., Liao, X., Fu, H., et al., 2025b. Interaction behaviors between finite-scale natural and hydraulic fractures in hot dry rock geothermal systems. Phys. Fluids 37, 26614. https://doi.org/10.1063/5.0252814.

Huang, L., Liao, X., Fu, H., et al., 2024. Interplay mechanisms between hydraulic fractures and natural fractures in various propagation regimes. Phys. Fluids 36, 106628. https://doi.org/10.1063/5.0234922.

Huang, L., Liu, J., Zhang, F., et al., 2019. Exploring the influence of rock inherent heterogeneity and grain size on hydraulic fracturing using discrete element modeling. Int. J. Solid Struct. 176–177, 207–220. https://doi.org/10.1016/j.ijsolstr.2019.06.018.

Huang, L., Tan, J., Fu, H., et al., 2023. The non-plane initiation and propagation mechanism of multiple hydraulic fractures in tight reservoirs considering stress shadow effects. Eng. Fract. Mech. 292, 109570. https://doi.org/10.1016/j.engfracmech.2023.109570.

Li, J., Wang, L., Feng, C., et al., 2024. Study on the influence of perforation parameters on hydraulic fracture initiation and propagation based on CDEM. Comput. Geotech. 167, 106061. https://doi.org/10.1016/j.compgeo.2023.106061.
Li, Y., Hubuqin, Wu, J., et al., 2023. Optimization method of oriented perforation parameters improving uneven fractures initiation for horizontal well fracturing. Fuel 349, 128754. https://doi.org/10.1016/j.fuel.2023.128754.
Liang, H., Pei, J., Guo, S., et al., 2023. Performance simulation and perforated parameters optimize for perforated wells with compaction zone and drilling damage in tight gas reservoirs. J. Eng. Res. 11, 100062. https://doi.org/10.1016/j.jer.2023.100062.
Liu, H., Lan, Z., Wang, S., et al., 2015. Hydraulic fracture initiation mechanism in the definite plane perforating technology of horizontal well. Petrol. Explor. Dev. 42, 869–875. https://doi.org/10.1016/S1876-3804(15)30084-7.
Liu, Q., Li, J.L., Liang, B., et al., 2023. Complex wettability behavior triggering mechanism on imbibition: A model construction and comparative study based on analysis at multiple scales. Energy 275, 127434. https://doi.org/10.1016/j.energy.2023.127434.
Liu, S., Zhang, D., Liu, H., 2020. Rock crack propagation mechanism of oriented perforation hydraulic fracture under different perforation parameters. Arabian J. Sci. Eng. 45, 8711–8725. https://doi.org/10.1007/s13369-020-04821-y.
Lu, W., Bai, E., Wei, L., et al., 2022. Numerical simulation on spatial steering rule of directional perforation hydraulic fractures in low-permeability reservoir. Front. Earth Sci. 10, 1007218. https://doi.org/10.3389/feart.2022.1007218.
Luo, C., Jia, A., Guo, J., et al., 2016. Analysis on effective reservoirs and length optimization of horizontal wells in the Sulige gasfield. Nat. Gas. Ind. B 3, 245–252. https://doi.org/10.1016/j.ngib.2016.05.009.
Michael, A., Gupta, I., 2021. A comparative study of oriented perforating and fracture initiation in seven shale gas plays. J. Nat. Gas Sci. Eng. 88, 103801. https://doi.org/10.1016/j.jngse.2021.103801.
Moukhtari, F.E., Lecampion, B., 2018. A semi-infinite hydraulic fracture driven by a shear-thinning fluid. J. Fluid Mech. 838, 573–605. https://doi.org/10.1017/jfm.2017.900.
Patel, S., Wilson, I., Sreenivasan, H., et al., 2024. Numerical simulations of proppant transportation in cryogenic fluids: implications on liquid helium and liquid nitrogen fracturing for subsurface hydrogen storage. Int. J. Hydrogen Energy 56, 924–936. https://doi.org/10.1016/j.ijhydene.2023.12.268.
Pereira, L., Lecampion, B., 2021. A plane-strain hydraulic fracture driven by a shear-thinning Carreau fluid. Int. J. Numer. Anal. Methods GeoMech. 45, 1603–1623. https://doi.org/10.1002/nag.3216.
Pidho, J.J., Cheng, Y., Yan, C., 2022. Investigation of interference from multiple oriented hydraulic fractures while considering near-radial wellbore stress distribution. J. Nat. Gas Sci. Eng. 103, 104625. https://doi.org/10.1016/j.jngse.2022.104625.
Pucknell, J.K., Behrmann, L.A., 1991. An investigation of the damaged zone created by perforating. In: SPE Annual Technical Conference and Exhibition. https://doi.org/10.2118/22811-MS.
Ren, L., Jiang, H., Zhao, J., et al., 2022. Theoretical study on fracture initiation in deep perforated wells with considering wellbore deformation. J. Pet. Sci. Eng. 211, 110141. https://doi.org/10.1016/j.petrol.2022.110141.
Shi, X., Han, L., Han, Q., et al., 2021. Experimental near-wellbore hydraulic fracture initiation and growth for horizontal wells with in-plane perforations. J. Nat. Gas Sci. Eng. 95, 104224. https://doi.org/10.1016/j.jngse.2021.104224.
Tang, J., Wang, X., Du, X., et al., 2023. Optimization of integrated geological-engineering design of volume fracturing with fan-shaped well pattern. Petrol. Explor. Dev. 50, 971–978. https://doi.org/10.1016/S1876-3804(23)60442-2.
Tang, J., Zhang, M., Guo, X., et al., 2024. Investigation of creep and transport mechanisms of $CO_2$ fracturing within natural gas hydrates. Energy 300, 131214. https://doi.org/10.1016/j.energy.2024.131214.
Wang, H., Li, M., Wang, B., et al., 2024. Study on hydraulic fracture propagation behavior from oriented perforation based on particle flow method. Int. J. Energy Res. 2024, 8876708. https://doi.org/10.1155/2024/8876708.
Wang, J., Zhao, Z., Li, D., et al., 2023. Research on a novel liquid-solid phase change self-supporting fracturing fluid system. Geoenergy Sci. Eng. 231, 212323. https://doi.org/10.1016/j.geoen.2023.212323.
Wang, X., Feng, Y., Zhang, F., et al., 2025. Investigation on breakage and collapse characteristics of hard and thick roof during coal excavation subject to hydraulic fracturing. Eng. Fail. Anal. 181, 109935. https://doi.org/10.1016/j.engfailanal.2025.109935.
Wang, X., Tang, M., Du, X., et al., 2023a. Three-dimensional experimental and numerical investigations on fracture initiation and propagation for oriented limited-entry perforation and helical perforation. Rock Mech. Rock Eng. 56, 437–462. https://doi.org/10.1007/s00603-022-03069-2.
Wang, X., Zhang, F., Tang, M., et al., 2023b. Numerical investigation of hydraulic fracture deflection in large-angle oblique horizontal wells with staged multi-cluster fracturing. Geoenergy Sci. Eng. 222, 211436. https://doi.org/10.1016/j.geoen.2023.211436.
Wang, X., Zhang, F., Tang, M., et al., 2022a. Effect of stress shadow caused by multistage fracturing from multiple well pads on fracture initiation and near-wellbore propagation from infill wells. SPE J. 27, 204–225. https://doi.org/10.2118/208577-PA.
Wang, X., Zhang, F., Yin, Z., et al., 2022b. Numerical investigation of refracturing with/without temporarily plugging diverters in tight reservoirs. Pet. Sci. 19, 2210–2226. https://doi.org/10.1016/J.PETSCI.2022.05.006.
Wang, X., Zhang, F., Zhu, H., et al., 2026. Numerical simulation on fracture propagation of multilayer combined fracturing in coal-bearing strata: analyzing perforation design effects. Eng. Fract. Mech. 332, 111807. https://doi.org/10.1016/j.engfracmech.2025.111807.
Wu, J., Huang, H., Xu, E., et al., 2021. Numerical investigation on propagation behaviors of a three-dimensional fracture network coupled with microseismicity in fractured shale reservoirs. Energies 14, 8297. https://doi.org/10.3390/en14248297.
Xi, X., Yang, S., Shipton, Z., et al., 2022. Modelling the near-wellbore rock fracture tortuosity: role of casing-cement-rock well system, perforation and in-situ stress. Int. J. Rock Mech. Min. Sci. 157, 105182. https://doi.org/10.1016/j.ijrmms.2022.105182.
Xia, K., Cui, Y., Mahmood, T., 2025. A novel oriented perforation approach for fracturing deep and tight reservoirs. Rock Mech. Rock Eng. 58, 107–122. https://doi.org/10.1007/s00603-024-03846-1.
Yan, Y., Guan, Z., Yan, W., et al., 2020. Mechanical response and damage mechanism of cement sheath during perforation in oil and gas well. J. Pet. Sci. Eng. 188, 106924. https://doi.org/10.1016/j.petrol.2020.106924.
Yin, Z., Zhang, F., Wang, X., et al., 2025a. Four-dimensional stress induced by hydraulic fracturing and long-term extraction for shale gas well platforms: implications for refracturing design. J. Rock Mech. Geotech. Eng. https://doi.org/10.1016/j.jrmge.2025.07.025.
Yin, Z., Zhang, Y., Zhang, F., et al., 2025b. Dynamic evolution mechanisms of induced stresses in hydraulically fractured wells: incorporating real gas characteristics. Int. J. Rock Mech. Min. Sci. 195, 106298. https://doi.org/10.1016/j.ijrmms.2025.106298.
You, S., Liao, Q., Yue, Y., et al., 2025. Enhancing fracture geometry monitoring in hydraulic fracturing using radial basis functions and distributed acoustic sensing. Adv. Geo-Energy Res. 16, 260–275. https://doi.org/10.46690/ager.2025.06.06.
Zafarian, H., Ameri, M., Vaghasloo, Y.A., et al., 2021. Error reduction of tracking planned trajectory in a thin oil layer drilling using smart rotary steerable system. J. Pet. Sci. Eng. 196, 107668. https://doi.org/10.1016/j.petrol.2020.107668.
Zeng, F., Peng, F., Zeng, B., et al., 2019. Perforation orientation optimization to reduce the fracture initiation pressure of a deviated cased hole. J. Pet. Sci. Eng. 177, 829–840. https://doi.org/10.1016/j.petrol.2019.02.080.
Zhang, B., Gamage, R.P., Kong, L., et al., 2025a. Cross-scale proppants transport in the shale hydraulic fracture network: a hybrid CFD-DEM investigation. Eng. Geol. 354, 108160. https://doi.org/10.1016/j.enggeo.2025.108160.
Zhang, F., Wan, H., Liu, B., et al., 2025. Numerical simulation on the influence of natural fractures on hydraulic fracture propagation in fractured coal reservoirs. Energy Fuel. 39, 1938–1958. https://doi.org/10.1021/acs.energyfuels.4c05177.
Zhang, F., Wang, X., Tang, M., et al., 2021. Numerical investigation on hydraulic fracturing of extreme limited entry perforating in plug-and-perforation completion of shale oil reservoir in Changqing oilfield, China. Rock Mech. Rock Eng. 54, 2925–2941. https://doi.org/10.1007/s00603-021-02450-x.
Zhang, R., Wang, L., Li, J., et al., 2024. Numerical analysis of perforation during hydraulic fracture initiation based on continuous–discontinuous element method. Comput. Model. Eng. Sci. 140, 2103–2129. https://doi.org/10.32604/cmes.2024.049885.
Zhang, R., Zhang, X., Kang, T., et al., 2020. Dynamic fracture propagation model for oriented perforation steering fracturing in low permeability reservoir based on microelement method. J. Nat. Gas Sci. Eng. 74, 103105. https://doi.org/10.1016/j.jngse.2019.103105.
Zhang, T., Tang, T., Guo, J., et al., 2023. Quantitative testing method of solid-liquid two-phase for unconventional fracturing proppant transport. Flow Meas. Instrum. 93, 102431. https://doi.org/10.1016/j.flowmeasinst.2023.102431.
Zhang, Z., Tang, J., Zhang, J., et al., 2024. Modeling of scale-dependent perforation geometrical fracture growth in naturally layered media. Eng. Geol. 336, 107499. https://doi.org/10.1016/J.ENGGEO.2024.107499.
Zhao, H., Li, X., Zhen, H., et al., 2023. Study on H-shaped fracture propagation and optimization in shallow dull-type coal seams in the Hancheng block, China. Geoenergy Sci. Eng. 221, 111226. https://doi.org/10.1016/j.petrol.2022.111226.
Zhou, H., Yan, T., Trivedi, J., et al., 2025. Investigating rock properties and fracture propagation pattern during supercritical $CO_2$ pre-fracturing in conglomerate reservoir. Adv. Geo-Energy Res. 17, 95–106. https://doi.org/10.46690/ager.2025.08.02.
Zhou, J., Yan, D., Yao, M., et al., 2025. Effect of flexible fibers for preventing proppant flowback after fracture closure by CFD-DEM method. Geoenergy Sci. Eng. 247, 213719. https://doi.org/10.1016/j.geoen.2025.213719.